A&A 476, 89–96 (2007)
DOI: 10.1051/0004-6361:20066824

Astronomy
&
Astrophysics

Narrow-band Hβ images of star-formation regions in HII galaxies[⋆],[⋆⋆]

P. Lagos[1], E. Telles[1], and J. Melnick[2]

[1] Observatório Nacional, Rua José Cristino 77, 20.921-400 Rio de Janeiro – RJ, Brazil
e-mail: `[plagosl;etelles]@on.br`
[2] European Southern Observatory, Alonso de Cordova 3107, Santiago, Chile
e-mail: `jmelnick@eso.org`

Received 27 November 2006 / Accepted 26 June 2007

ABSTRACT

Aims. Create a catalog of images of HII galaxies and their individual star-formation regions in order to study the distribution of the gas emission and their underlying stellar continuum.

Methods. We have used Hβ narrow-band images of 43 selected HII galaxies obtained at ESO NTT 3.58 m telescope using the SUSI2 camera.

Results. Surface photometric Hβ fluxes and equivalent widths for all objects and star-formation regions are presented in this catalog. A myriad of filamentary structure were found in the pure Hβ emission-line or continuum-subtracted images, probably attributed to expanding shells as a consequence of the star-formation activity. Our results indicate that the number of regions with high Hβ equivalent width or young regions increase with the instrumental resolution, showing that the instrumental resolution is a bias to determine the cluster ages. Therefore, we showed that some of the observed giant HII regions may have been formed by ensembles of unresolved star forming regions or candidates to host Super Star Clusters. Pure Hβ emission-line images, continuum contours and EW(Hβ) maps showing the morphology of the gaseous and stellar emission in HII galaxies and their individual star-formation regions were obtained. All calibrated continuum and Hβ emission line fluxes and the derived Hβ equivalent width images are available in fits format from `http://www.on.br/astro/etelles/HIIgalaxies/Hbeta/`.

Key words. catalogs – galaxies: dwarf – galaxies: photometry – galaxies: ISM – galaxies: fundamental parameters

1. Introduction

HII galaxies are low-luminosity ($M_B \geq -18$), metal poor (between 1/50 and 1/3 $Z_{\odot}$) and compact objects (~1 kpc) with intense star-formation activity, showing HII region like spectra (Sargent & Searle 1970; Thuan & Martin 1981), and faint, blue optical continua. Some of these galaxies are called Blue Compact Dwarf galaxies (BCD) when selected by their blue colors instead of their strong emission lines. Initially it was hypothesized that HII galaxies were young galaxies forming their first generation of stars. However, optical and NIR photometry (Thuan 1983; Telles 1995; Papaderos et al. 1996a,b; Telles & Terlevich 1997a; Cairós et al. 2003) revealed the existence of underlying populations of old stars suggesting an intermittent star-formation history with short intense star-forming episodes followed by long quiescent phases. More recently, Westera et al. (2004) have used stellar absorption indices to infer the presence of intermediate and old populations of stars in these galaxies. The presence of an underlying stellar continuum from previous events of star formation will affect the observed EW(Hβ) which will not be a pure measure of the age of the present burst, but then will be a measure of the age of the present star formation episode weighed by the whole past history of star formation of the underlying galaxy, as was noted by Terlevich et al. (2004). Yet, HII galaxies are relatively simple systems compared to more massive galaxies, in the sense that they do not show conspicuous spiral arms in disky structure, but show a rich variety of overall morphologies from roundish regular to typically more irregular shapes (Telles et al. 1997a). The star formation regions may show single or multiple knots with complex internal structure, generally consisting of unresolved emsembles of Super Star Clusters (SSCs) and the effects of their evolution on the distribution of the interstellar medium.

Self-propagation and cyclic gas infall have been invoked to explain the star-formation activity in these galaxies. The lack of external perturbers and spiral structures in these galaxies indicates that an additional mechanism other than tidal interactions and density waves must be considered to explain their strong star-formation rates in a relative small physical size. The internal mechanism which may trigger star formation in these galaxies without an obvious external agent is yet unknown, but may be related to the overall physical conditions of the ISM, particularly the gas surface densities, in conjunction with stochastic effects, allowing star formation to pop up simultaneously over kiloparsec scales. Once star formation is initiated then the collective winds and supernova ejecta from young stellar associations or Super Stars Clusters take over to propagate star formation in scales of a tens of parsec to few hundred parsec as observed in giant HII regions and individual star forming knots (e.g., Tenorio-Tagle & Bodenheimer 1988; Elmegreen 1992; Tenorio-Tagle et al. 2006, and reference therein). This scenario of star formation may be

---

[⋆] Based on observations made with ESO NTT 3.5 m Telescope at the La Silla Observatory under programmen ID ⟨68.B – 0678(A)⟩ and ⟨70.B – 0184(A)⟩.

[⋆⋆] Tables 1, 3 and Figs. 4, 5 are only available in electronic form at `http://www.aanda.org` invoked to explain the observed distribution of chemical abundances in HII galaxies. These huge expanding shells sweep up the ISM, dispersing the metals (Tenorio-Tagle 1996) formed in the current star-formation episode in scales of 10^2-10^3 pc and timescales less than 10^7 yr. Eventually the shells expand into the halo and deform and break due to Rayleigh-Taylor instabilities, but the metal production cannot be completely lost. How much metals are lost or kept in a hot phase before it is mixed in the ISM and observed in the warm phase, is an essential issue for our understanding of the recycling process and chemical evolution in dwarf galaxies (Lagos et al. 2006, 2007, in preparation).

While there are a few spectroscopic catalogs containing data for hundreds of HII galaxies, (Terlevich et al. 1991; Kehrig et al. 2004, and references therein), narrow-band images of these objects are not very common; for example, Telles (1995) observed a sample of 11 HII galaxies using Hα narrow-band images to calculate the integrated properties of these systems. Gil de Paz et al. (2003) analyzed B and R broadband and Hα narrow-band images of 105 BCD galaxies, and Cairós et al. (2001) observed 28 galaxies using B, V, R, I and Hα images. However, none of these studies spatially resolved the contributions of individual star-forming regions within the parent galaxies.

In this paper we study narrow-band images (Hβ and continuum) of a sample of 43 HII galaxies in order to identify the ensembles of star-formation regions within each galaxy, thus revealing the morphology and structure of the ionized gas, and creating catalogs of the individual giant HII region components. For each galaxy we present fluxes and EW(Hβ) of each star-formation region as well as the integrated values, and we also present EW(Hβ) maps that illustrate the relative age-distributions of the star-forming regions. Hβ was used in this work instead of the usual Hα because the latter is contaminated by [NII] emission in narrow band affecting the accuracy of photometry, and because we also wish to evaluate our surface photometry with slit spectrophotometry commonly used in parametric studies to quantify possible observational biases.

In Sect. 2 we describe the observations and data reduction methods. Section 3 describes the flux calibration procedure. The results and discussions are showed in Sect. 4. Finally, we summarize our results in Sect. 5.

2. Observation and data reduction

The data presented in this work were obtained on March 14, 2002 and March 30–April 01, 2003 at the ESO NTT 3.58 m telescope in La Silla Chile, using the SUSI2 (Superb Seeing Imager-2) camera.The SUSI2 detector is a 2 CCDs array of 1024×2048 pixels each, covering an extended area on the sky of $5\farcm5 \times 5\farcm5$. This camera has a pixel scale of $0\farcs161$ pixel^{-1} in the 2×2 binned mode.

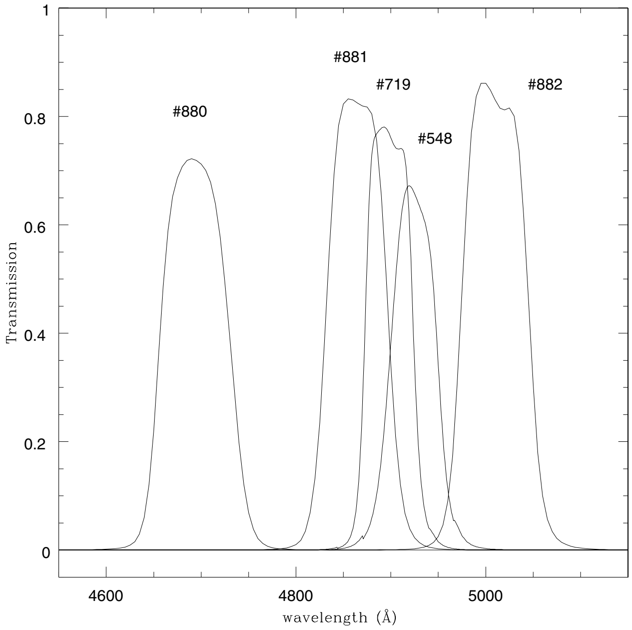

Fig. 1. Transmitions curves for narrow-bands filters 548, 719, 880, 881 and 882 used at the NTT telescope on La Silla.

Table 2. Properties of narrow-band filters. Column (1) indicates the corresponding number in the ESO filter catalogs. Column (2) central wavelength value. Column (3) list the $FWHM$ in Å, Col. (4) the Transmission of the filters and Col. (5) is the extinction coefficient for the filters calculated using the average curve for the atmospheric extinction at La Silla.

Filter (1)	λ_c (Å) (2)	$FWHM$ (Å) (3)	T % (4)	K_λ (Mag/airmass) (5)
548	4924.15	52.14	67.22	0.137
719	4898.24	51.62	78.04	0.140
880	4693.51	76.44	72.20	0.161
881	4864.38	66.68	83.23	0.147
882	5009.84	72.44	86.12	0.129

Our sample consists of 43 HII galaxies of the catalog of HII Galaxies of Terlevich et al. (1991), galaxies discovered in objective prism surveys: Tololo survey (Smith et al. 1976; Maza et al. 1991), the University of Michigan survey (Salzer et al. 1989), Markarian surveys (Markarian et al. 1981, 1986) and the Marseille Schmidt surveys (Surace & Comte 1998). The objects used in this study were selected because they appear compact in broad-band images showing one or some intense star-formation regions, ideal targets for high quality and high spatial resolution instruments like SUSI2. Our objective is to resolve star forming knots and identify individual emsembles of SSCs, not observed in previous works using narrow-band images. In Table 1 we show the sample of galaxies and the observation log, here Col. (1) gives the galaxy name, Cols. (2) and (3) give their coordinates, Col. (4) presents the redshift from NED[1], Cols. (5)–(7) give the filter number, the exposure time and the date of the observation, respectively. Finally, Col. (8) shows the seeing of the observations measured as the gaussian $FWHM$ of stellar images. In Col. (6) HBNB means Hβ Narrow-Band and CONT means Continuum.

The filter numbers 548, 719, 881 and 882 for the narrow-band (Hβ+continuum) images and the narrow-band filter 880 (He II) for the continuum (filter adjacent in wavelength to the Hβ emission) were used. In Fig. 1 we present the spectral response function and in Table 2 the specification for these filters, indicating the corresponding number in the ESO filter catalogs (Col. 1), the central wavelength in Å (Col. 2), the $FWHM$ in Å (Col. 3), the transmission of the filters (Col. 4) and the extinction coefficient performed using the average curve for the atmospheric extinction at La Silla (Col. 5). For each galaxy two or three Hβ+continuum images and one or two continuum images were taken. Twilight flat-fields were taken for each filter and night as well as standard stars for flux calibration.

---

[1] NASA/IPAC Extragalactic Database (NED) which is operated by the Jet Propulsion laboratory, California Institute of technology, under contract with the National Aeronautics and Space Administration.

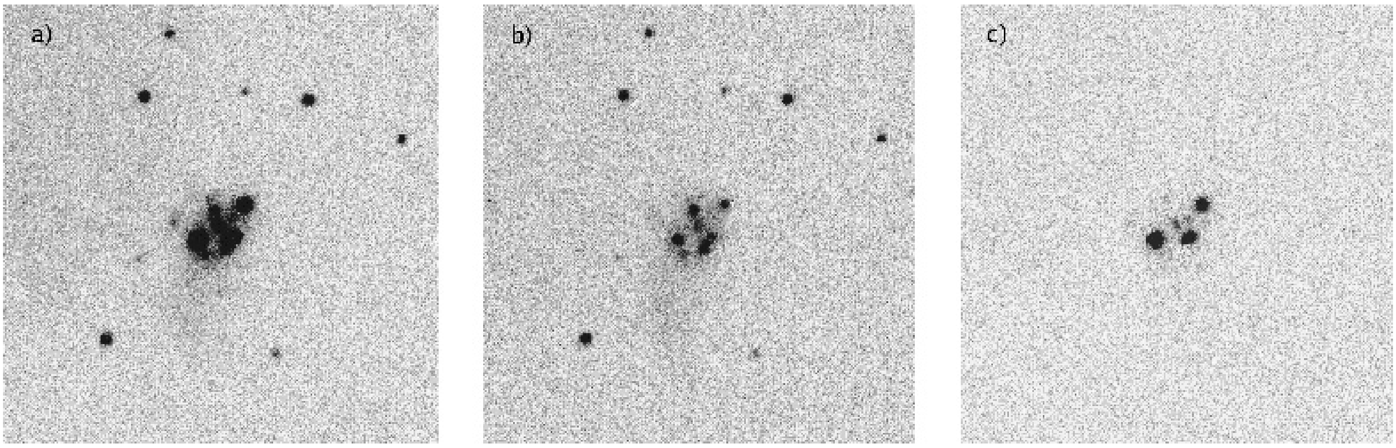

Fig. 2. Galaxy Tol 1334-326. Continuum subtraction procedure. **a)** Hβ+continuum image, **b)** continuum image and **c)** continuum-subtracted image. The continuum-subtracted image (frame **c)**) was obtained scaling the continuum image (frame **b)**) in relation to the Hβ+continuum image (frame **a)**) until the average flux of a non saturated field stars were equal in both images. This scaled image was then subtracted from the Hβ+continuum image to produce a continuum-subtracted Hβ emission line image.

The images were reduced following the standard procedure of bias and flat-fielding correction, using the IRAF[2] task CCDPROC. In most cases, it was necessary an alignment of the images, transforming geometrically each pixel. This procedure was done using the IMALIGN task. The cosmic rays were removed combining two or three images using IMCOMBINE or using IMEDIT when only one image was available.

3. Flux calibration and measurement

In order to obtain flux calibrated images, we have followed the method of Jacoby et al. (1987). For a standard star, the total observed flux in the narrow-band filter I in [erg s^{-1} cm^{-2}] assuming the stellar energy distribution (SED) constant, is given by

$$F(I) = \int F_\lambda T(I) \mathrm{d}\lambda = F_\lambda \int T(I) \mathrm{d}\lambda, \quad (1)$$

where $T(I)$ is the transmission curve for the filter I that in our case corresponds to the filters in Fig. 1 and F_λ is the monochromatic flux above the atmosphere for the standard star in units of [erg s^{-1} Å^{-1} cm^{-2}]. The CCD system sensitivity is given by

$$S(I) = \frac{F(I)}{C 10^{0.4Xk(I)}}\cdot \quad (2)$$

Here $k(I)$ is the extinction coefficient for the filter I performed using the average curve for the atmospheric extinction at La Silla, X is the air mass and C the count rate.

The total flux above the atmosphere for a narrow-band (NB) galaxy image, is given by

$$F(I)_{\mathrm{galaxy}} = \int F(I)_{\mathrm{NB},\lambda} T(I)_\lambda \mathrm{d}\lambda = F(I)_{\mathrm{NB}} T(I). \quad (3)$$

The sensitivity of the system is similar to Eq. (2), then combining Eqs. (2) and (3) we obtain the calibrated flux image for a galaxy, that is given by

$$F(I)_{\mathrm{galaxy}} = \frac{C_{\mathrm{NB}}}{T(I)} 10^{0.4Xk(I)} \langle S(I) \rangle, \quad (4)$$

where $\langle S(I) \rangle$ is the average value of the sensitivity of the system derived from several standard stars.

In some cases, the combined or total narrow-band and continuum images for a same object and run of observation have different seeing, then using the task GAUSS of IRAF we convolved the combined images of each object with a Gaussian kernel to match the worst seeing image. We show in Table 1 final seeing used in the flux calibration procedure.

The continuum-subtracted Hβ images resulting in a pure Hβ line emission image, were obtained by scaling the continuum image in relation to the Hβ+continuum until the average fluxes of non-saturated field stars were equal in both frames. This scaled image was then subtracted from the Hβ+continuum image to produce the continuum-subtracted Hβ emission line image. The same procedure was made for all galaxies in the sample, except in Mrk 36 where only two field stars were found. Therefore, the continuum-subtracted image in this galaxy was obtained scaling the low surface brightness regions. In Fig. 2 we see the continuum-subtracted procedure to the galaxy Tol 1334-326, where Fig. 2a is the original narrow-band image or Hβ+continuum, Fig. 2b is the continuum image and Fig. 2c the continuum-subtracted Hβ image. We emphasize that the continuum image is a pure narrow-band continuum image and thus the continuum-subtracted image is a pure nebular emission image.

The total flux for each galaxy was measured using the IRAF task POLYPHOT. The local background on each of these galaxies was measured, in order to calculate the mean background level, thus the background was subtracted from each pixel. The Hβ continuum-subtracted and continuum fluxes were measured using polygonal and elliptical apertures. Finally, the Hβ equivalent width was found as follows: we calculated the ratio between the continuum-subtracted and continuum fluxes for each galaxy and star-formation region and then multiplying this ratio by the *FWHM* of the narrow-band filter (see Table 2). All calibrated continuum and Hβ emission line fluxes and the derived Hβ equivalent width (*EW*(Hβ)) images in fits format are available from `http://www.on.br/astro/etelles/HIIgalaxies/Hbeta/`.

We have calculated the Hβ luminosity adopting the logarithmic extinction coefficient by Kehrig et al. (2004) and Terlevich et al. (1991) from the Balmer decrements Hα/Hβ, and the coefficients given by Peña et al. (1991), Telles et al. (2001) and

---

[2] IRAF: the Image Reduction and Analysis Facility is distributed by the National Optical Astronomy Observatories, which is operated by the Association of Universities for Research in Astronomy, In. (AURA) under cooperative agreement with the National Science Foundation (NSF).

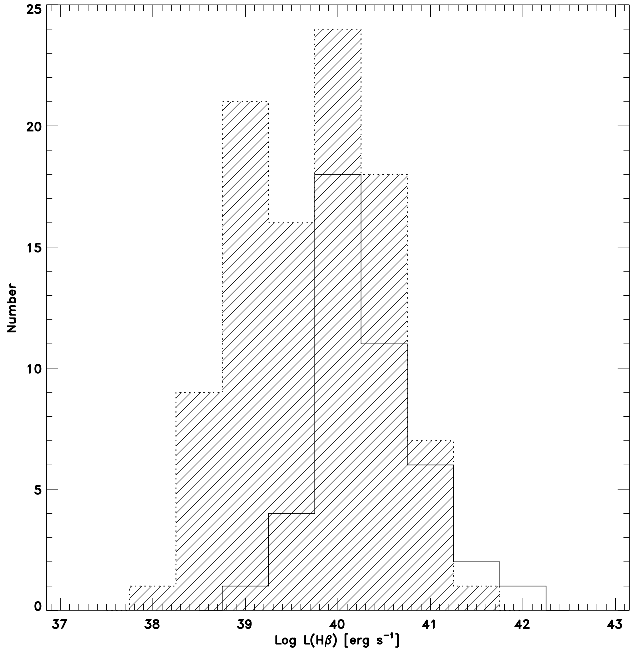

Fig. 3. Distribution of the Hβ luminosity. Solid line represent the distribution for the integrated values and dashed line the distribution for the star-formation regions.

Telles et al. (1997b), assuming the same value for the integrated galaxies and star-formation regions. In Fig. 3 we show the resultant luminosity histogram of the sample. In Table 3 we show the observed properties of the sample, where columns: (1) give the name of the galaxy, (2) show the observed Hβ fluxes in units of $\times 10^{-14}$ erg s^{-1} cm^{-2}, (3) the Hβ luminosity in units of erg s^{-1}, (4) Hβ equivalent width in units of Å, (5) the morphologycal classification given by [1] Loose & Thuan (1986) and [2] Telles et al. (1997b) based in broad-band images, and finally in (6) we present the adopted extinction coefficient c(Hβ). The errors shown in Table 3 were estimated using the errors in the sensitivity function obtained from the observation of several standard stars and propagated along of the calibration and continuum substraction procedure. Typically the errors are $\lesssim$15% of the total flux to integrated galaxies and $\lesssim$50% to star-formation regions. Distances were computed assuming a Hubble constant of H_0 = 71 km s^{-1} Mpc^{-1}.

4. Results and analysis

4.1. Morphology of the galaxies

Figure 4 shows continuum-subtracted Hβ emission-line images using a logarithmic stretch. The continuum fluxes are shown in contours. Color *EW*(Hβ) maps are found in the electronic edition of this journal in Fig. 5 (online material). For all images North is to the top and East to the left. The axes units are arcsec. A few residual foreground stars in the maps are removed, except when they are very close to the galaxies as in Tol 1147-283, Tol 1334-326, Tol 1457-262, Tol 1924-416, Tol 1937-423 and Tol 2019-405.

Two different morphological classification schemes have been used in the literature. Loose & Thuan (1986) have used broad-band images to classify their sample of BCD galaxies into four groups: (i) iE – galaxies with an outer diffuse halo and elliptical isophotes, and inner irregular isophotes due to the presence of multiple star formation regions and star clusters; (ii) nE – galaxies with a elliptical halo and a well defined nucleus; (iii) iI – objects with an irregular outer halo and off-center nucleus presenting different configurations; iI,C – cometary morphology; iI,M – apparent mergers; and (iv) i0 – galaxies that do not show a diffuse extended component. Telles et al. (1997b) divided their HII galaxies into two groups: type I – luminous galaxies with a distorted morphology, and type II – low luminosity, regular and compact galaxies. Both classification schemes used broad band images. Gil de Paz et al. (2003) observed that in some cases, despite the regular shape of the continuum isophotes in the inner region, the Hα images showed complex structures, thus completely changing the morphologies of these galaxies. We have used both the continuum images (images obtained using the filter 880) in order to classify the galaxies in our sample in terms of the underlying galaxy, unaffected by line emission, and the Hβ images (filters centered on the redshifted Hβ line). The latter will allow us to identify the morphology of the line emitting regions and how much these are affecting the overall morphology usually observed in broad band images. Column (5) of Table 3 shows the morphological classification of our sample of galaxies based on the Loose & Thuan (1986) and Telles et al. (1997b) criteria. We found 21 galaxies in the sample (∼50%) with only one star-formation region in the Hβ image. Of these, 8 galaxies (IIZw40, Tol 1025-285, CTS 1016, UM 455, UM 463, UM 559, CTS 1034 and IIZw70) show filamentary structures or a coma like structure which might suggest a violent evolution of the ISM, contributing to the morphology of the star forming region. The 22 remaining galaxies show multiple regions with more or less strong signs of disturbances in the ISM. 44% of the galaxies are cataloged as type I, and the reminder as type II. Using the Loose & Thuan (1986) criteria we find that 35% are type iE, 44% are type nE, 9% iI,C, 7% are iI,M and 5% are type i0. It is clear that Telles et al. (1997b) criteria emcompasses Loose & Thuan (1986) criteria but with less emphasis on the morphology of the starburst component.

HII galaxies are generally isolated objects, without an excess of bright or dwarf companions (Telles & Terlevich 1995; Telles & Maddox 2000, and references therein). Telles & Maddox (2000) found that the tidal interaction cannot be the only factor to trigger the star-formation activity in these galaxies, because HII galaxies do not have preferentially more faint neighbors than other galaxies. Despite the apparent isolation of HII galaxies, the analysis of the emission and continuum images in some galaxies of our sample has revealed some signs of interaction at least in the galaxies: IIZw40 and Tol 0633-415. For example, in the Hβ image of IIZw 40 we can observe an intense central star-formation region. The continuum contours show a secondary region just below the brightest one. This galaxy is cataloged as iI,M (apparent merger) galaxy using the Loose & Thuan (1986) classification and as type I using the Telles et al. (1997b) classification. There are two elongated structures in the South-East direction of the galaxy, suggestive of a merger of two galaxies in progress. Some kinematic evidence, supporting this idea, is given by Van Zee et al. (1998). A detailed kinematics analysis of the central region of this galaxy is given by Bordalo et al. (2007). However, the question remains, if HII galaxies are isolated, and one supposes the star formation is observed during a merger in progress, why does one not observe pre-merging phases, such as an excess of very close companions?

The internal morphology of the starburst is also an interesting issue, once it shows the strong effect of the mechanical energy, winds and photoionization, of the newly born massive stars over the ISM (Tenorio-Tagle et al. 2006). One for instance can note the filamentary structures generally very close to the clusters, to distances that range from ∼100 pc to ∼1000 pc. We have

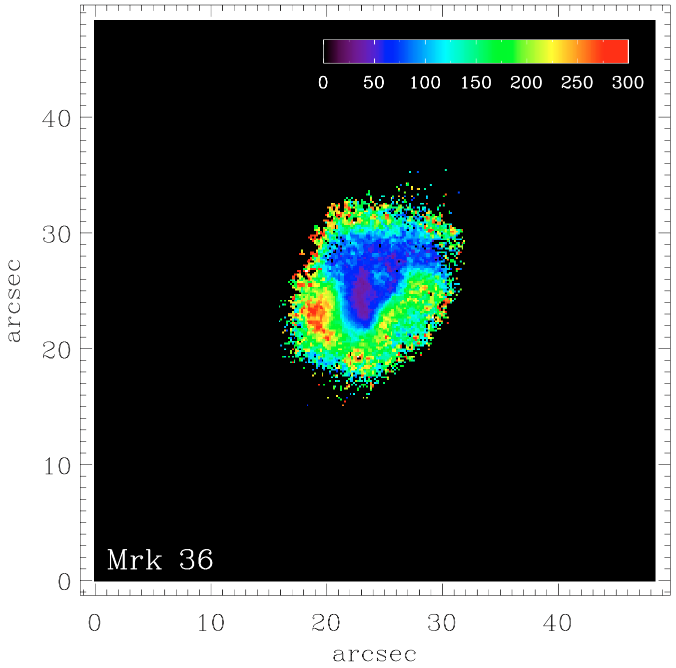

Fig. 6. Hβ equivalent width map of the galaxy Mrk 36. The colorbar is in units of Å. North is to the top and East to the left.

found these filamentary structures in the galaxies with multiples star-formation regions: Tol 0957-278, Tol 1004-296, Mrk 36, UM 456, UM 462, UM 483, IIZw 70 and Tol 1924-416. Some interesting case are discussed as follow:

In the galaxy Tol 1004-296, classified as iE galaxy, we can observe two main intense star-formation regions with blobby internal sub-structures, one in the center of the galaxy and the other one in the South-East direction. In the continuum contour we see a star, very close to the galaxy in the South-West position of the image. The Hβ map shows a myriad of filamentary structures and an extended faint emission or ionized gas in the outer part of the galaxy. A bipolar outflow structure extending out from the nuclear region of the galaxy is detected in our images in the same way as Hα observations by Marlowe et al. (1995). A faint Hβ emission is detected over the extension of the galaxy UM 439, connecting the star-formation regions, these structures are appreciated more easily in the EW(Hβ) map of the galaxy. The galaxy UM 462 shows eight star-formation regions and a number of shells possibly related with propagating star-formation in scales of up to a few hundred parsec.

Figure 6 shows an example of a Hβ equivalent width map (EW(Hβ)) of a well known HII galaxy Mrk 36, originally considered a bonafide example of a young compact object. The continuum isophotes of Mrk 36 in Fig. 4 are elongated, showing two peaks in the central part of the galaxy. The Hβ image shows two star-formation regions (≥100 pc of diameter) and a net of filamentary structures departing from these regions. Within the filamentary structures, we can observe regions with large equivalent width values, places where the star-formation activity has possibly just been triggered.

Finally, in some cases where the center of line emission is not coincident with the continuum, we see that the displacement is symmetric around the continuum center as in the galaxies Tol 0957-278, CTS 1013, Tol 1025-285, CTS 1020, Mrk 36, Tol 1147-283, [SC98] 13228-2547, IIZw 70 and Tol 2019-405 or not symmetric as in the galaxies [SC98] 13191-2212 and Tol 1937-423.

4.2. Photometry results

Our catalog of narrow band surface photometry of 43 galaxies is designed to sample the full range of Hβ luminosities and equivalent widths covered by larger spectroscopic surveys. Table 3 presents our observed fluxes F(Hβ), luminosities L(Hβ), and equivalent widths EW(Hβ) for the integrated galaxies and each star-formation region. The numbers below each galaxy in Table 3 represent the different regions, indicated in Fig. 4. Figure 7 compares our integrated surface photometric F(Hβ) and EW(Hβ) with those in common with the slit spectrophotometry of Kehrig et al. (2004, K04) and Terlevich et al. (1991, T91). The solid and dashed lines in Fig. 7 represents a 0% (1 to 1) and 60% differences between our values and the cataloged spectroscopic values. The photometric fluxes are about ~60% brighter than the spectroscopic fluxes, indicating that the slit position and the aperture in the spectroscopic surveys may introduce critical observational biases. One may expect that these apertures effects will be less severe for high redshift objects for their apparently smaller angular sizes. Comparing our integrated data of EW(Hβ) with the data of Kehrig et al. (2004) (40 objects in common) we found good agreement with this catalog. The agreement between our data and the Terlevich et al. (1991) (26 objects in common) data is overall reasonable but with larger scatter. The fact that the surface photometric EW(Hβ) statistically agrees with the slit spectrophotometric EW(Hβ) means that the nebular emission typically covers most of the observed extension of this type of galaxy. In Fig. 7d, the galaxy UM 559 deviates most of the general trend for its overall morphology with a single star forming region in one end over an extended stellar component.

The average value of Log EW(Hβ) is 1.62 (~42 Å) with a standard deviation of 0.41 for the integrated galaxies and 1.78 (~60 Å) for the star-formation regions with a standard deviation of 0.36 in units of [Å].

The difference beetwen the photometric and spectroscopic fluxes will also reflect directly in the luminosity values, therefore affecting the spread of the L(Hβ)-σ relation (Terlevich & Melnick 1981). In a second paper we will analyze the L(Hβ)-σ relation for our sample of HII galaxies. In Fig. 3 we showed the luminosity histogram of the sample. The average values are Log L(Hβ) = 40.30 for the integrated galaxies and Log L(Hβ) = 39.72 for the star-formation regions, with a standard deviation of 0.56 and 0.75 respectively (in units of [erg s^{-1}]).

4.3. The EW(Hβ) distribution

It is important to note that less than 10% of the galaxies in Terlevich et al. (1991) have EW(Hβ) > 150 Å contrary to model predictions (e.g., Terlevich et al. 2004, and reference therein). Several explanations have been proposed for the lack of systems with very high EW(Hβ) in the Terlevich et al. (1991) and Kehrig et al. (2004) samples: an important amount of ionizing photons are escaping from the star-formation regions (Cuisinier et al. 2006); the presence of an underlying old population of stars; uncertainties with the models; or low spatial resolution in the observational data. This last point, the spatial distribution of the star-formation knots, can also contribute biasing the measured EW(Hβ) value used as a current burst age indicator (Dottori 1981; and Copetti et al. 1986) in starburst galaxies.

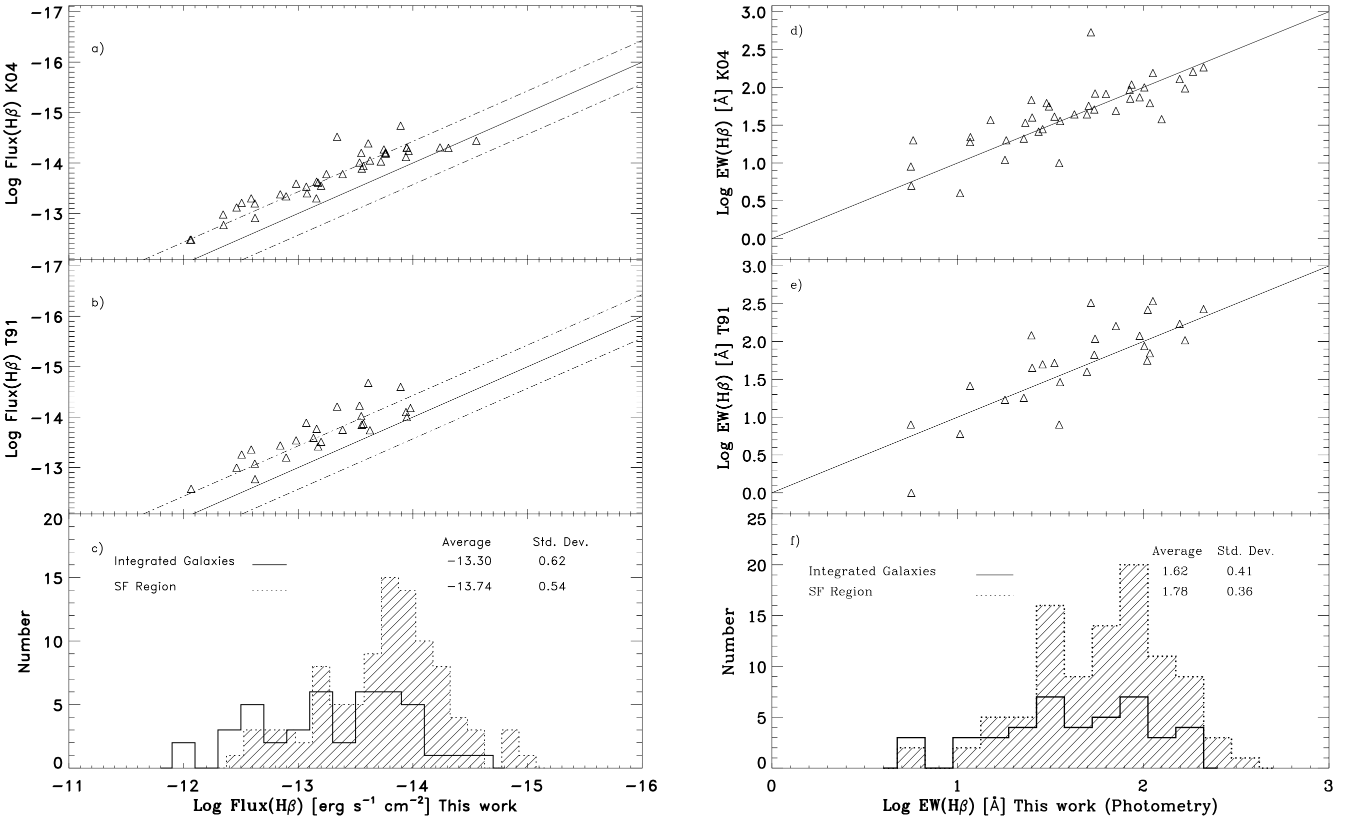

Fig. 7. a) Comparison of the Hβ integrated flux of our sample with those in common with K04. **b)** Comparison of the Hβ integrated flux of our sample with those in common with T91. **c)** Distribution of Hβ fluxes for the integrated galaxies (solid line) and star-formation regions (dashed line). **d)** Comparison of the integrated *EW*(Hβ) of our sample with those in common with K04 **e)** Comparison of the integrated *EW*(Hβ) of our sample with those in common with T91 **f)** Distribution of *EW*(Hβ) for the integrated galaxies (Solid line) and star-formation regions (dashed line). Fluxes in units of [erg s^{-1} cm^{-2}] and *EW*(Hβ) in units of Å. Solid and dashed lines in figures **a)**, **b)**, **d)** and **e)** represents a 0% (1 to 1) and 60% differences between our values and the cataloged spectroscopic values.

Table 4. Statistical properties of the sample. The index R mean values to star-formation region and int mean integrated values. F(Hβ) are in unit of [erg s^{-1} cm^{-2}], L(Hβ) are in units of [erg s^{-1}] and EW(Hβ) in units of [Å].

	Average	std
Log $F(\mathrm{H}\beta)_{\mathrm{int}}$	–13.30	0.62
Log $F(\mathrm{H}\beta)_{\mathrm{R}}$	–13.74	0.54
Log $L(\mathrm{H}\beta)_{\mathrm{int}}$	40.30	0.56
Log $L(\mathrm{H}\beta)_{\mathrm{R}}$	39.72	0.75
Log $EW(\mathrm{H}\beta)_{\mathrm{int}}$	1.62	0.41
Log $EW(\mathrm{H}\beta)_{\mathrm{R}}$	1.78	0.36

Our observations indicate that the number of regions with high Hβ equivalent widths (high *EW*(Hβ) values correspond to young objects) increases when we measure the contribution of the individual regions (see Fig. 7f), showing that the instrumental resolution is a bias to determine the cluster ages. However, unless our individual components are themselves unresolved clumps of even smaller clusters, our observations reduce, but do not fully explain the lack of high equivalent widths expected by the single-burst population synthesis models. Therefore, the presence of underlying population of old(er) stars is still required to explain the observed distribution of *EW*(Hβ). Figure 7f shows *EW*(Hβ) distribution of star-formation regions when those multiple components are measured. We note that the average log *EW*(Hβ) is shifted from ~42 Å to ~60 Å, representing an age decrease of ~0.31, 0.28 and 0.44 Myr with respect to the integrated objects, for an instantaneous burst and a Salpeter IMF for a mass limit 1 $M_{\odot}$ to 100 $M_{\odot}$ and $Z = 0.004$, 0.008 and 0.020 as given by STARBURST99 (Leitherer et al. 1999).

In some cases, this type of young objects have been identified in the literature as SSCs or YMCs (Young Massive Clusters). Some classical examples are “Antennae” NGC 4038/39 (Whitmore & Schweizer 1995), NGC 7252 (Whitmore et al. 1993), and NGC 1569 and NGC 1705 (O’Connell 1994). Super Star Clusters are known as objects with high luminosity and compact sizes (~1−10 pc of radii) with ages <10 Myr and masses of 10^{3-6} $M_{\odot}$.

Figure 8 plots L(Hβ) vs. EW(Hβ) for all our galaxies (big filled circles) and individual star-forming regions (small filled circles). The continuous lines represent the model predictions of Stasinska & Leitherer (1996) for O/H = 2.13×10^{-5} and $n = 10$ cm^{-3} and ages between 1 and 10 Myr, for three values for the total mass of the burst: 10^3, 10^6, and 10^9 $M_{\odot}$. From Fig. 8 we note that most of our star-forming knots may consist of candidate SSC with masses between 10^3 $M_{\odot}$ to 10^6 $M_{\odot}$, the same range of mass estimated in other galaxies, such as in NGC 1569, M 82 (Melo et al. 2005) and the HII galaxy UM 462 (Vanzi 2003). It is possible that younger clusters are still unresolved and the measured *EW*(Hβ) are an average value of the ensemble of individual

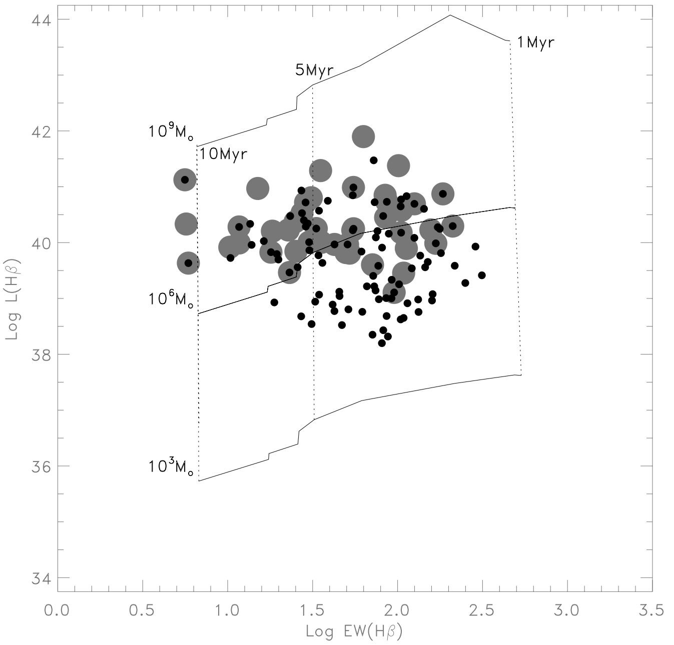

Fig. 8. Hβ luminosity vs. *EW*. for all sample of galaxies (big filled circles) and star forming regions (small filled circles). The grid of lines represents the model prediction by Stasinska & Leitherer 1996 for O/H = 2.13×10^{-5} and $n = 10$ cm^{-3} for ages between $1-10 \times 10^6$ yrs (dashed lines), considering the three values for the total initial mass M of the burst of those models 10^3, 10^6 and 10^9 $M_\odot$ (solid lines).

clusters. In any case, our results suggest that the massive star formation mode in starburst is intimately related to the formation of SSCs, rather independently of the triggering mechanism.

In addition, Vanzi et al. (2002) observed three representative low metallicity ($<Z_\odot/6$) galaxies Tol 35, Tol 3 and UM 462, in order to study the NIR colors and spectra of the star-formation regions. They found a sequential trend in the observed colors, interpreted as an age gradient as result of propagating star-formation, possibly triggered by supernovae explotions. Star formation propagation is, however, only likely within individual large knots, or in scales less than ~100 pc. It is unlikely that propagation occurs in galactic scales. Alternatively, the overall surface density over kiloparsec scales may be responsible for the triggering of star-formation in a stochastic manner.

5. Conclusions

We have presented high spatial resolution Hβ narrow-band images and photometric properties of 43 HII galaxies and their star-forming regions, where we have derived Hβ pure emission-line images, continuum contours and *EW*(Hβ) maps showing the morphology of the HII galaxies and their individual star-formation regions. From these, we present some concluding points:

1. The Hβ equivalent width maps clearly show that HII galaxies have intense star-formation activity over large extensions, spread in blobby, knotty structures.
2. Using spectroscopic values of the extinction from the literature we present Hβ luminosities integrated over the whole galaxies, and for the individual star-formation region. We obtain an average value of Log L(Hβ) = 40.30 [erg s^{-1}] for the integrated flux of our sample, and Log L(Hβ) = 39.72 [erg s^{-1}] for all the star-formation regions. This is larger than the typical GHRs in other local group galaxies and may indicate that these regions found in HII galaxies are scaled up analogues to GHRs.
3. A myriad of filamentary structures are revealed by the continuum-subtracted (line emission) images akin to those observed in nearby Giant HII Regions. This similarity indicates that expanding supershells are shaping the ISM also in HII galaxies.
4. The number of regions with large Hβ equivalent widths increase with spatial resolution, showing that resolution is an important bias in the determination of the cluster ages. Therefore, we can assume that some of the giant HII region components in our galaxies may still be formed by ensembles of unresolved stellar cluster and some of them are real candidates to be Super Star Clusters or Young Massive clusters. Given that even in our sample there is an important discrepancy between the observed Hβ equivalent widths, and the values predicted by single burst models, it would be crucial to observe some of the largest individual components in our sample using even higher spatial resolutions either from space, or from the ground using adaptive optics instruments, in order to identify the elementary entities that constitute the starburst.

Acknowledgements. P.L. acknowledges support from CNPq and Faperj, Brazil for his studentship. We would also like to thank the anonymous referee for his/her comments which substantially improved the paper.

References

Bordalo, V., Plana, H., & Telles, E. 2007, ApJ, submitted
Cairós, L. M., Vilchez, J. M., González Pérez, J. N., Iglesias-Páramo, J., & Caon, N. 2001, ApJS, 133, 321
Cairós, L. M., Caon, N., Papaderos, P., et al. 2003, ApJ, 593, 312
Copetti, M. V. F., Pastoriza, M. G., & Dottori, H. A. 1986, A&A, 156, 111
Cuisinier, F., Westera, P., Telles, E., & Buser, R. 2006, A&A, 455, 825
Doublier, V., Mas-Hesse, J. M., Caulet, A., & Kunth, D. 2001, A&A, 372, 22
Dottori, H. A. 1981, Ap&SS, 80, 267
Elmegreen, B. G. 1994, ApJ, 427, 384
Elmegreen, B. G. 1992, Star formation in stellar systems, ed. G. Tenorio-Tagle, M. Prieto, & F. Sánchez (Cambridge University Press)
Gil de Paz, A., Madore, B. F., & Pevunova, O. 2003, ApJS, 147, 29
Jacoby, G. H., Africano, J. L., & Quigley, R. J. 1987, PASP, 99, 672
Kehrig, C., Telles, E., & Cuisinier, F. 2004, AJ, 128, 1141 (K04)
Kunth, D., & Sargent, W. L. W. 1983, A&A, 273, 81
Kunth, D., & Sargent, W. L. W. 1986, A&A, 101, 5
Lagos, P., Telles, E., Carrasco, R., & Cuisinier, F. 2006, RMxAC, 26, 193
Lagos, P., Telles, E., Muñoz-Tuñón, C., et al. 2007, in preparation
Leitherer, C., Schaerer, D., Goldader, J. D., et al. 1999, ApJS, 123, 3
Loose, H.-H., & Thuan, T. X. 1986, ApJ, 309, 59
Markarian, B. E., Lipovetskii, V. A., & Stepanian, D. A. 1981, Astrofizika, 17, 619
Markarian, B. E., Stepanian, D. A., & Erastova, L. K. 1986, Astrofizika, 25, 345
Marlowe, A. T., Heckman, T. M., Wyse, R. F. G., & Schommer, R. 1995, ApJ, 438, 563
Maza, J., Ruiz, M. T., Gonzalez, L. E., Wischnjewsky, M., & Pena, M. 1991, A&AS, 89, 389
Melo, V. P., Muñoz-Tuñón, C., Maiz-Apellániz, J., & Tenorio-Tagle, G. 2005, ApJ, 619, 270
O'Connell, R. W., Gallagher III, J. S., & Hunter, D. A. 1994, ApJ, 433, 65
Papaderos, P., Loose, H. H., Thuan, T. X., & Fricke, K. J. 1996a, A&AS, 120, 207
Papaderos, P., Loose, H. H., Fricke, K. J., & Thuan, T. X. 1996b, A&A, 314, 59
Peña, M., Ruiz, M. T., & Maza, J. 1991, A&A, 251, 417
Sargent, W. L. W., & Searle, L. 1970, ApJ, 162, 155

Salzer, J. J., MacAlpine, G. M., & Boroson, T. A. 1989, ApJS, 70, 447
Smith, M. G., Aguirre, C., & Zemelman, M. 1976, ApJS, 32, 217
Stasinska, G., & Leitherer, C. 1996, ApJS, 107, 661
Surace, C., & Comte, G. 1998, A&AS, 133, 171
Taylor, C. L. 1997, ApJ, 480, 524
Telles, E. 1995, Ph.D Thesis, Univ. Cambridge
Telles, E., & Terlevich, R. 1995, MNRAS, 275, 1
Telles, E., & Terlevich, R. 1997a, MNRAS, 286, 183
Telles, E., Melnick, J., & Terlevich, R. 1997b, MNRAS, 288, 78
Telles, E., & Maddox, S. 2000, MNRAS, 311, 307
Telles, E., Muñoz-Tuñón, C., & Tenorio-Tagle, G. 2001, ApJ, 548, 671
Tenorio-Tagle, G. 1996, AJ, 111, 1641
Tenorio-Tagle, G., & Bodenheimer, P. 1988, ARA&A, 26, 146
Tenorio-Tagle, G., Muñoz-Túñon, C., Pérez, E., Silich, S., & Telles, E. 2006, ApJ, 643, 186
Terlevich, R., & Melnick, J. 1981, MNRAS, 195, 839
Terlevich, R., Melnick, J., Masegosa, J., Moles, M., & Copetti, M. V. F. 1991, A&AS, 91, 285 (T91)
Terlevich, R., Silich, S., Rosa-González, D., & Terlevich, E. 2004, MNRAS, 348, 1191
Thuan, T. X. 1983, ApJ, 268, 667
Thuan, T. X., & Martin, G. E. 1981, ApJ, 247, 823
Westera, P., Cuisinier, F., Telles, E., & Kehrig, C. 2004, A&A, 423, 133
Whitmore, B. C., & Schweizer, F. 1995, ApJ, 109, 960
Whitmore, B. C., Schweizer, F., Leitherer, C., Borne, K., & Robert, C. 1993, ApJ, 106, 1354
Vanzi, L. 2003, A&A, 408, 523
Vanzi, L., Hunt, L. K., & Thuan, T. X. 2002, A&A, 390, 481
Van Zee, L., Skillman, E. D., & Salzer, J. J. 1998, AJ, 116, 1186

Online Material

Table 1. Sample and log of observation. Column (1) give the galaxy name. Columns (2) and (3) give their coordinates. Column (4) represent the redshift obtained from NED. Columns (5)–(7) give the Filter number, the exposure time and the date of observation, respectively. Column (8) shows the seeing to each observations, it was measured as the *FWHM* of stellar images. In Col. (6) HBNB means Hβ Narrow-Band and CONT mean Continuum.

	Galaxy (1)	α(2000) (2)	δ(2000) (3)	z (4)	Filter number (5)	Exposure Time (s) (HBNB – CONT) (6)	Date of observation (7)	seeing (″) (8)
1	Tol 0505-387	05:07:00.8	–38:38:58	0.0300	882	2 × 600 – 1 × 600	2003 March 30	1.1
2	Tol 0528-383	05:29:57.4	–38:18:07	0.0110	719	2 × 600 – 1 × 600	2003 April 01	1.1
3	IIZw 40	05:55:38.3	+03:24:24	0.0026	881	2 × 600 – 2 × 600	2002 March 14	1.1
4	Tol 0610-387	06:12:14.2	–38:46:23	0.0060	881	2 × 600 – 1 × 600	2003 March 31	1.1
5	Tol 0633-415	06:35:09.7	–41:33:29	0.0170	548	2 × 600 – 1 × 600	2003 March 30	1.4
6	Tol 0645-376	06:46:50.1	–37:43:21	0.0260	882	2 × 600 – 1 × 600	2003 March 30	1.4
7	Cam 0840+1044	08:42:36.5	10:33:13	0.0120	719	2 × 600 – 1 × 600	2002 March 14	1.1
8	Tol 0957-278	09:59:21.0	–28:08:00	0.0032	719	2 × 600 – 1 × 600	2002 March 14	1.0
9	Tol 1004-296	10:06:33.0	–29:56:08	0.0037	881	2 × 600 – 1 × 600	2002 March 14	0.9
10	CTS 1011	10:19:21.2	–22:08:35	0.0121	548	2 × 900 – 2 × 450	2003 March 31	1.1
11	CTS 1013	10:25:05.9	–19:46:57	0.0264	882	2 × 600 – 2 × 300	2003 March 31	1.1
12	Tol 1025-285	10:27:25.5	–28:47:32	0.0299	882	2 × 600 – 1 × 600	2003 March 30	1.4
13	CTS 1016	10:37:30.6	–24:08:41	0.0349	882	2 × 600 – 1 × 600	2003 April 01	0.8
14	CTS 1017	10:37:40.4	–25:58:00	0.0351	882	2 × 900 – 1 × 900	2003 April 01	0.8
15	CTS 1020	10:47:44.2	–20:57:48	0.0123	548	2 × 600 – 1 × 600	2003 April 01	0.8
16	CTS 1022	10:48:40.1	–19:26:56	0.0135	548	2 × 600 – 1 × 600	2002 March 14	0.8
17	Mrk 1271	10:56:09.0	+06:10:23	0.0034	881	2 × 600 – 2 × 300	2003 March 31	1.0
18	Mrk 36	11:04:44.0	29:07:48	0.0021	881	2 × 600 – 1 × 600	2002 March 14	1.6
19	UM 439	11:36:36.8	+00:48:58	0.0036	881	2 × 600 – 1 × 600	2003 March 31	0.9
20	Tol 1147-283	11:50:03.3	–28:40:18	0.0064	719	2 × 600 – 1 × 600	2003 March 30	1.2
21	UM 455	11:50:23.7	–00:31:42	0.0128	548	3 × 600 – 1 × 600	2003 March 30	1.3
22	UM 456	11:50:36.2	–00:34:02	0.0059	881	2 × 600 – 1 × 600	2003 April 01	0.9
23	UM 461	11:51:33.1	–02:22:22	0.0034	881	2 × 600 – 1 × 600	2002 March 14	0.9
24	UM 462	11:52:37.3	–02:28:10	0.0035	881	2 × 600 – 1 × 600	2003 April 01	0.7
25	UM 463	11:52:47.5	–00:40:08	0.0046	881	3 × 600 – 1 × 600	2003 March 31	0.9
26	UM 483	12:12:14.7	+00:04:20	0.0078	719	2 × 600 – 1 × 600	2003 April 01	0.6
27	Mrk 1318	12:19:09.8	03:51:17	0.0050	719	2 × 600 – 1 × 600	2002 March 14	0.7
28	Tol 1223-359	12:25:44.9	–36:12:36	0.0090	719	2 × 600 – 1 × 600	2002 March 14	0.7
29	[SC98] 13016-2236	13:04:15.2	–22:52:53	0.0096	719	2 × 600 – 1 × 600	2003 March 30	1.1
30	UM 559	13:17:42.8	–01:00:01	0.0041	881	2 × 600 – 1 × 600	2003 March 31	0.8
31	[SC98] 13191-2212	13:21:49.9	–22:28:31	0.0238	882	2 × 600 – 1 × 600	2003 April 01	0.9
32	[SC98] 13228-2547	13:25:33.0	–26:02:50	0.0148	548	2 × 600 – 1 × 600	2003 March 30	1.0
33	Tol 1334-326	13:37:15.2	–32:55:15	0.0121	548	2 × 600 – 1 × 600	2002 March 14	0.9
34	Tol 1345-420	13:48:22.1	–42:21:14	0.0080	719	2 × 600 – 1 × 600	2002 March 14	1.0
35	CTS 1034	14:19:32.4	–27:35:08	0.0224	882	2 × 600 – 1 × 600	2003 March 30	1.5
36	IIZW 70	14:50:56.5	+35:34:18	0.0039	881	2 × 600 – 1 × 600	2003 March 31	1.4
37	CTS 1035	14:57:09.7	–22:23:35	0.0284	882	2 × 600 – 1 × 600	2003 March 30,31	1.4–1.0
38	Tol 1457-262ab	15:00:26.6	–26:27:11	0.0168	548	2 × 600 – 1 × 600	2002 March 14	0.8
39	Tol 1457-262ce	15:00:26.6	–27:11:99	0.0168	548	2 × 600 – 1 × 600	2002 March 14	0.8
40	Tol 1924-416	19:27:58.2	–41:34:32	0.0094	719	2 × 600 – 1 × 600	2003 April 01	1.0
41	Tol 1937-423	19:40:58.6	–42:15:45	0.0091	719	2 × 600 – 1 × 600	2003 March 31	0.9
42	Tol 2019-405	20:23:06.2	–40:20:33	0.0150	548	2 × 600 – 1 × 600	2003 April 01	0.9
43	Tol 2041-394	20:44:50.8	–39:13:17	0.0260	882	2 × 600 – 1 × 600	2003 April 01	0.9

Table 3. Observed properties of the sample. Columns: (1) Galaxy name, (2) Observed Hβ flux in $\times10^{-14}$ erg s^{-1} cm^{-2}, (3) Hβ luminosity erg s^{-1}, (4) Hβ equivalent width in Å, (5) Morphologycal classification given by [1] Loose & Thuan (1986) and [2] Telles et al. (1997b) criteria, and Col. (6) give the extinction coefficient used in this work: ^{a} given by Kehrig et al. (2004), ^{b} given by Peña et al. (1991), ^{c} given by Terlevich et al. (1991), ^{d} Telles et al. (2001) and ^{e} Telles et al. (1997b).

	Galaxy (1)	F(Hβ) 10^{-14} [erg s^{-1} cm^{-2}] (2)	log L(Hβ) [erg s^{-1}] (3)	EW(Hβ) [Å] (4)	Morphology [1] – [2] (5)	extinction c(Hβ) (6)
1	Tol0505-387	4.58 ± 0.05	41.29	35	iE – II	0.35^{a}
	1	0.87 ± 0.04	40.57	35		
	2	1.32 ± 0.14	40.75	39		
2	Tol0528-383	2.92 ± 0.04	40.23	23	iE – I	0.35^{a}
	1	0.63 ± 0.24	39.56	26		
	2	1.20 ± 0.27	39.84	61		
3	IIZw40	34.47 ± 0.63	40.29	211	iI,M – I	0.60^{a}
4	Tol0610-387	1.28 ± 0.04	39.91	10	iE – II	0.92^{a}
	1	0.09 ± 0.03	38.76	62		
	2	0.13 ± 0.02	38.92	33		
	3	0.82 ± 0.13	39.72	10		
	4	0.13 ± 0.04	38.92	19		
5	Tol0633-415	6.32 ± 0.11	40.99	55	iI,M – II	0.40^{a}
6	Tol0645-376	2.37 ± 0.12	40.72	29	nE – II	0.19^{a}
7	Cam0840+1044	1.73 ± 0.03	39.96	43	iI,C – II	0.24^{a}
8	Tol0957-278	31.15 ± 1.40	40.00	36	iE – I	0.17^{a}
	1	5.07 ± 0.50	39.21	73		
	2	0.83 ± 0.02	38.43	82		
	3	1.96 ± 0.03	38.80	51		
	4	1.03 ± 0.02	38.65	108		
9	Tol1004-296	87.43 ± 2.90	40.76	31	iE – I	0.36^{a}
	1	19.86 ± 1.70	40.12	89		
	2	11.18 ± 2.70	39.87	81		
	3	1.64 ± 0.28	39.04	160		
10	CTS1011	5.68 ± 0.06	40.85	84	iE – II	0.60^{b}
	1	1.30 ± 0.04	40.21	76		
	2	1.00 ± 0.03	40.09	74		
	3	0.31 ± 0.02	39.58	77		
11	CTS1013	1.75 ± 0.03	40.69	126	nE – II	0.28^{b}
12	Tol1025-285	1.15 ± 0.04	41.12	6	nE – II	0.78^{a}
13	CTS1016	1.13 ± 0.03	40.53	27	nE – II	0.06^{b}
14	CTS1017	1.72 ± 0.03	40.87	185	i0 – II	0.22^{b}
15	CTS1020	8.38 ± 0.70	40.73	86	nE – II	0.30^{b}
16	CTS1022	1.90 ± 0.14	39.97	51	nE – II	0.10^{b}
17	Mrk 1271	23.79 ± 0.68	39.99	168	nE – II	0.22^{e}
18	Mrk36	25.70 ± 0.98	39.45	109	iE – I	0.07^{a}
	1	7.42 ± 0.12	38.91	114		
	2	3.81 ± 0.27	38.62	104		

Table 3. continued.

	Galaxy (1)	$F(\mathrm{H}\beta)$ 10^{-14} [erg s^{-1} cm^{-2}] (2)	log $L(\mathrm{H}\beta)$ [erg s^{-1}] (3)	$EW(\mathrm{H}\beta)$ [Å] (4)	Morphology [1] – [2] (5)	extinction c(Hβ) (6)
19	UM439	14.34 ± 1.52	39.65	71	iE – I	0.05[a]
	1	6.78 ± 0.30	39.32	250		
	2	0.75 ± 0.01	38.36	88		
	3	0.57 ± 0.25	38.25	81		
20	Tol1147-283	4.10 ± 0.07	39.86	25	nE – II	0.31[c]
	1	1.49 ± 0.27	39.42	72		
	2	0.69 ± 0.26	38.09	34		
21	UM455	2.82 ± 0.11	40.25	33	iI,C – II	0.26[e]
22	UM456	8.50 ± 0.90	39.85	50	iI,C – I	0.05[a]
	1	2.30 ± 0.35	39.28	102		
	2	1.41 ± 0.28	39.07	45		
	3	0.61 ± 0.02	38.70	27		
	4	1.69 ± 0.30	39.15	45		
	5	0.62 ± 0.02	38.71	86		
	6	0.43 ± 0.02	38.55	47		
	7	0.29 ± 0.01	38.38	71		
23	UM461	12.75 ± 1.10	39.90	113	iE – I	0.40[e]
	1	10.50 ± 0.3	39.81	180		
	2	1.56 ± 0.3	38.98	78		
24	UM462	45.14 ± 1.98	40.45	85	iE – I	0.38[e]
	1	1.47 ± 0.27	38.96	160		
	2	2.64 ± 0.37	39.22	66		
	3	2.23 ± 0.33	39.14	74		
	4	1.61 ± 0.28	39.00	92		
	5	5.53 ± 0.53	39.54	121		
	6	5.79 ± 0.54	39.56	145		
	7	6.16 ± 0.56	39.58	217		
	8	1.53 ± 0.28	38.98	132		
	9	0.92 ± 0.22	38.76	133		
25	UM463	2.79 ± 0.40	39.11	95	nE – II	0.01[c]
26	UM483	2.70 ± 0.05	39.99	12	nE – I	0.45[a]
	1	1.62 ± 0.40	39.77	34		
	2	0.16 ± 0.01	38.77	43		
27	Mrk1318	23.93 ± 1.43	40.37	25	iE – I	0.27[a]
	1	0.78 ± 0.02	38.89	41		
	2	12.27 ± 0.78	40.08	125		
	3	2.18 ± 0.33	39.33	92		
	4	0.35 ± 0.01	38.54	31		
28	Tol1223-359	6.91 ± 0.12	40.22	157	iI,M – I	0.15[a]
	1	3.47 ± 0.63	39.93	287		
	2	0.41 ± 0.03	39.00	86		
29	[SC98] 13016-2236	1.09 ± 0.04	39.47	23	nE – II	0.14[a]
30	UM559	10.43 ± 0.97	39.83	52	iI,C – I	0.26[c]
	1	4.18 ± 0.76	39.43	313		
31	[SC98] 13191-2212	0.49 ± 0.02	40.28	12	nE – II	0.51[a]

Table 3. continued.

	Galaxy	F(Hβ)	log L(Hβ)	EW(Hβ)	Morphology	extinction
		10^{-14} [erg s^{-1} cm^{-2}]	[erg s^{-1}]	[Å]	[1] – [2]	c(Hβ)
	(1)	(2)	(3)	(4)	(5)	(6)
32	[SC98] 13228-2547	1.79 ± 0.04	40.20	18	nE – II	0.28[a]
	1	0.48 ± 0.02	39.63	36		
	2	1.19 ± 0.26	40.02	16		
33	Tol1334-326	7.36 ± 0.47	40.58	106	iE – I	0.22[e]
	1	3.42 ± 0.78	40.25	177		
	2	0.87 ± 0.34	39.65	150		
	3	1.13 ± 0.37	39.77	136		
34	Tol1345-420	6.71 ± 0.60	40.22	55	nE – II	0.26[a]
35	CTS 1034	0.28 ± 0.02	39.62	6	nE – II	0.15[b]
36	IIZW70	21.80 ± 1.08	40.25	55	nE – I	0.40[d]
37	CTS 1035	0.58 ± 0.03	40.01	30	nE – II	0.01[b]
38	Tol1457-262ab	44.78 ± 1.08	41.84	63	iE – I	0.41[a]
	1	1.10 ± 0.23	40.23	29		
	2	1.24 ± 0.25	40.28	30		
	3	3.98 ± 0.45	40.79	55		
	4	2.52 ± 0.36	40.59	104		
	5	3.36 ± 0.41	40.71	105		
	6	16.85 ± 0.92	41.41	72		
	7	4.85 ± 0.50	40.87	27		
	8	1.69 ± 0.30	40.42	82		
39	Tol1457-262ce	6.95 ± 0.20	40.97	15	iE – I	0.35[a]
	1	1.87 ± 0.74	40.40	28		
	2	2.23 ± 0.24	40.48	23		
	3	1.61 ± 0.22	40.33	14		
	4	0.68 ± 0.21	39.96	14		
	5	0.46 ± 0.26	39.79	19		
40	Tol1924-416	85.90 ± 2.22	41.38	101	iE – I	0.17[e]
	1	24.45 ± 2.40	40.83	113		
	2	19.03 ± 1.00	40.72	73		
	3	14.48 ± 3.40	40.60	143		
	4	6.79 ± 1.00	40.28	172		
41	Tol1937-423	2.45 ± 0.06	40.33	6	nE – I	0.70[a]
	1	0.57 ± 0.08	39.70	20		
	2	0.83 ± 0.09	39.86	30		
42	Tol2019-405	1.13 ± 0.03	39.83	18	nE – II	0.10[a]
43	Tol2041-394	1.05 ± 0.02	40.18	105	i0 – II	0.00

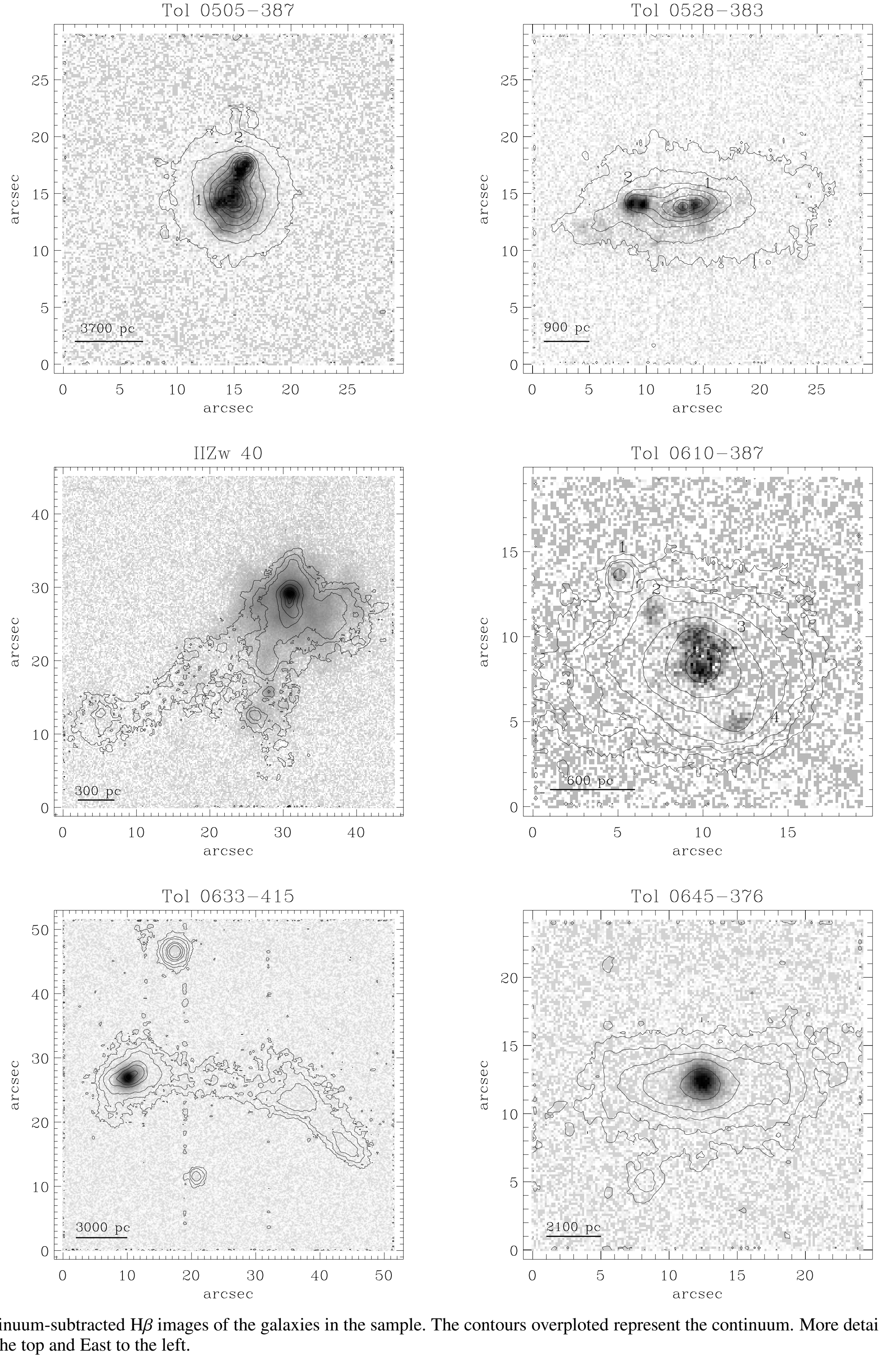

Fig. 4. Continuum-subtracted Hβ images of the galaxies in the sample. The contours overploted represent the continuum. More details in the text. North is to the top and East to the left.

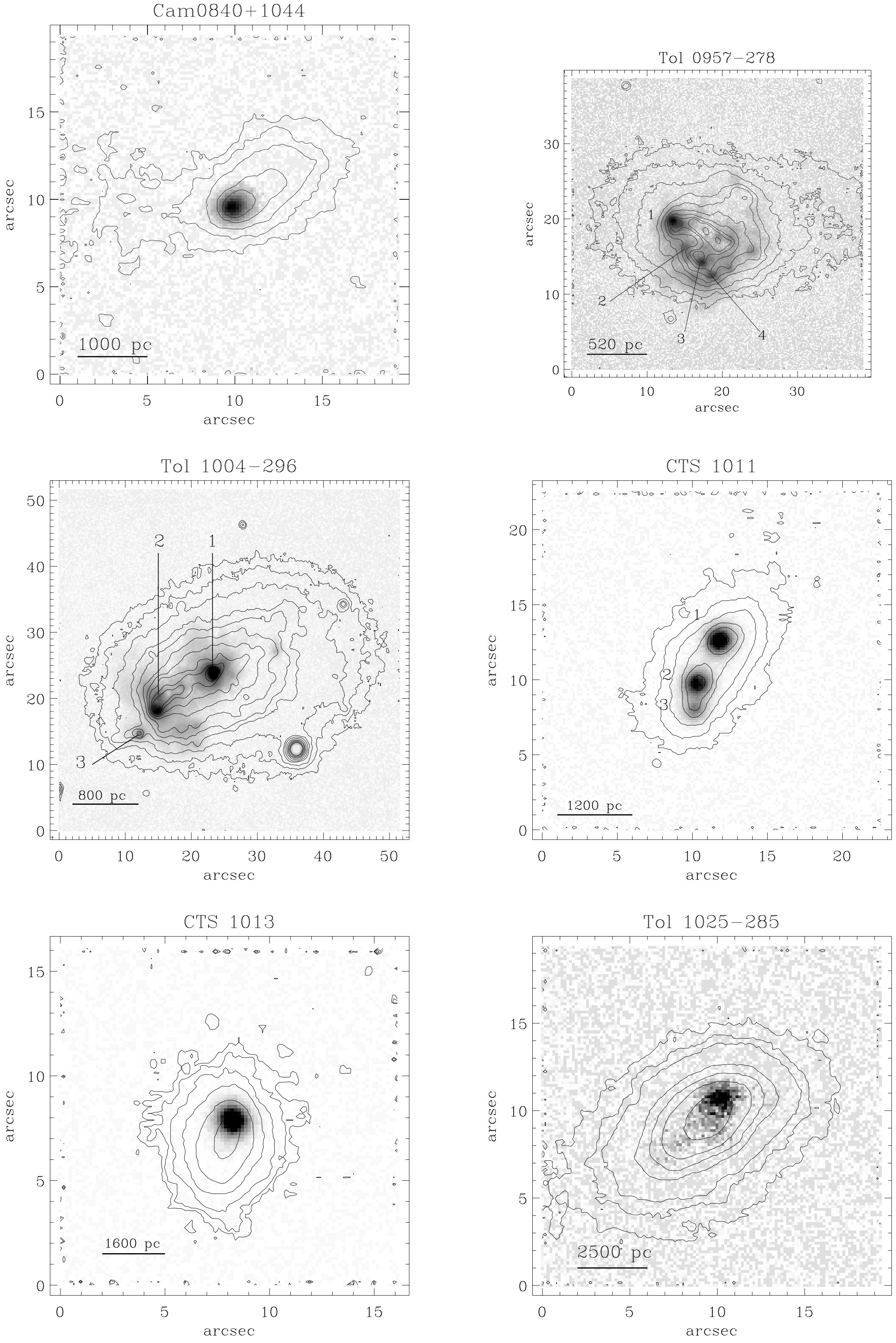

Fig. 4. continued.

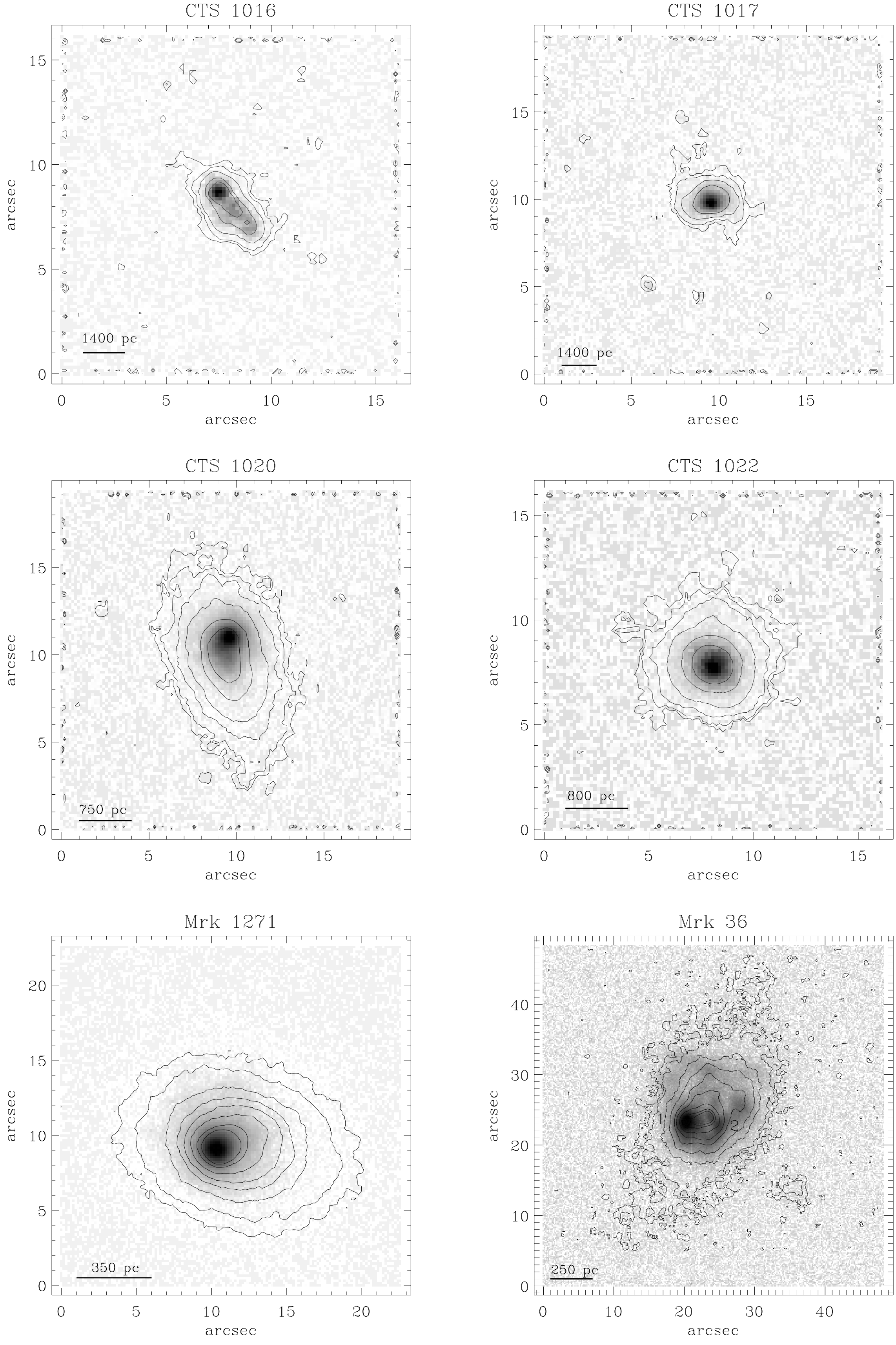

Fig. 4. continued.

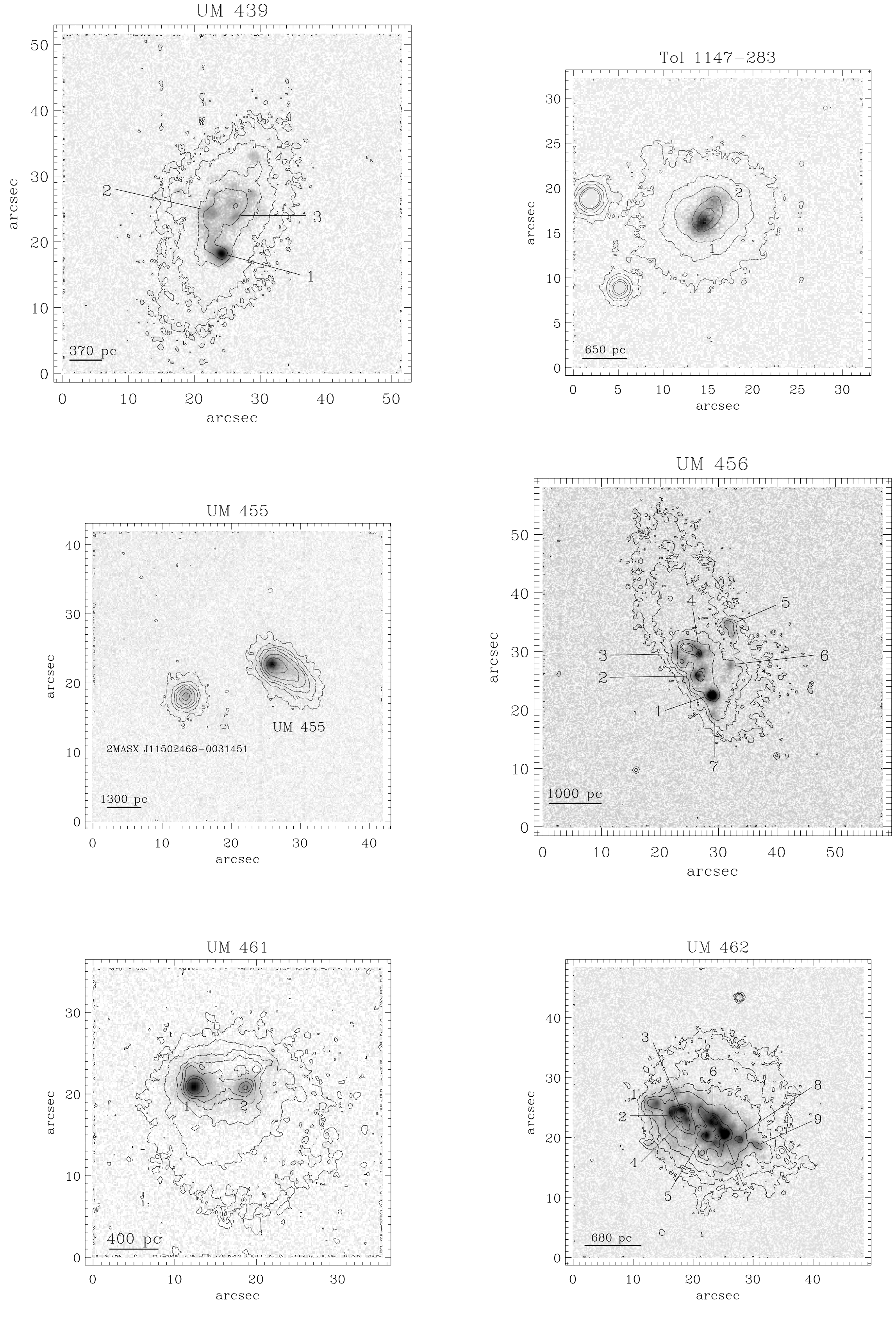

Fig. 4. continued.

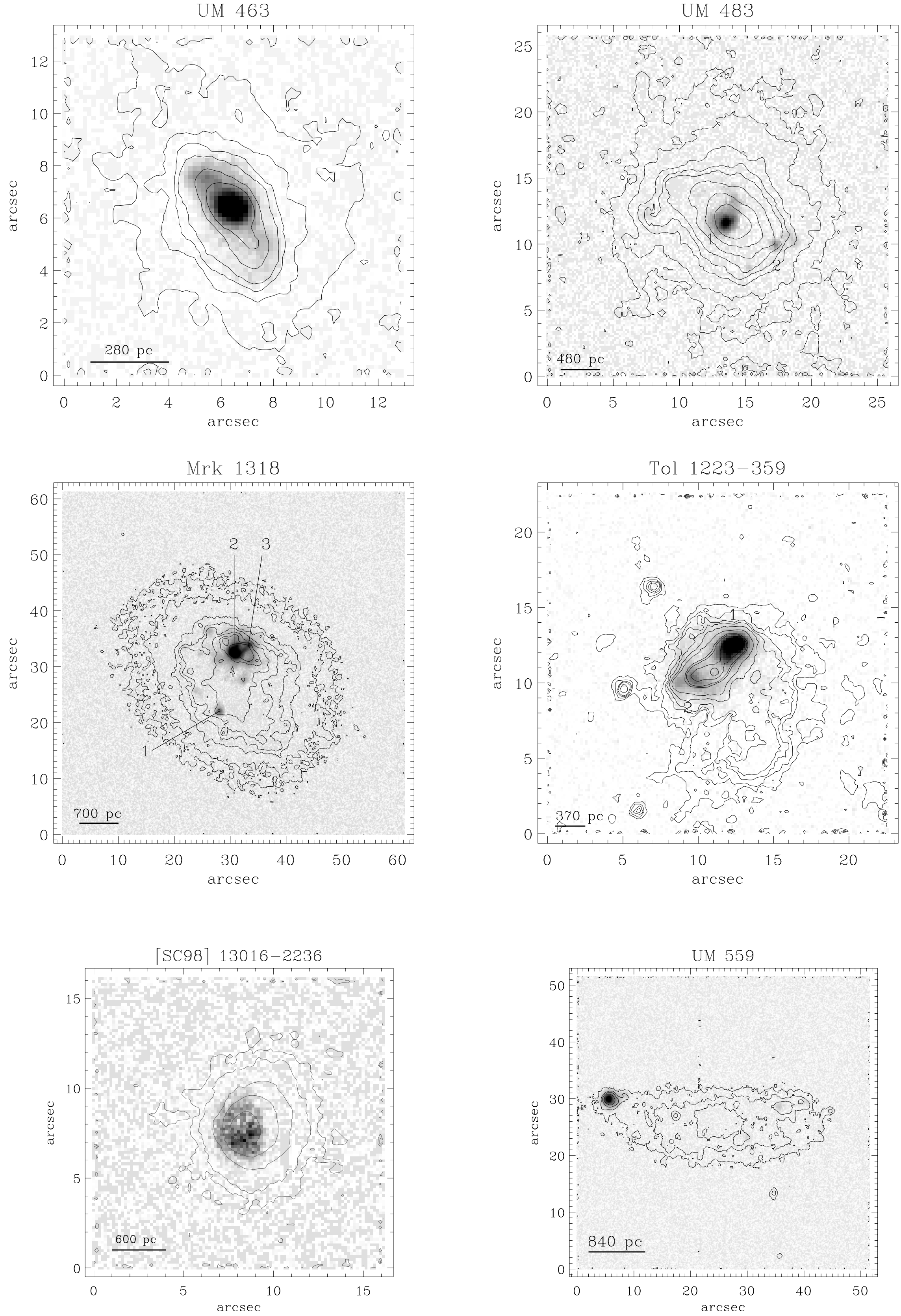

Fig. 4. continued.

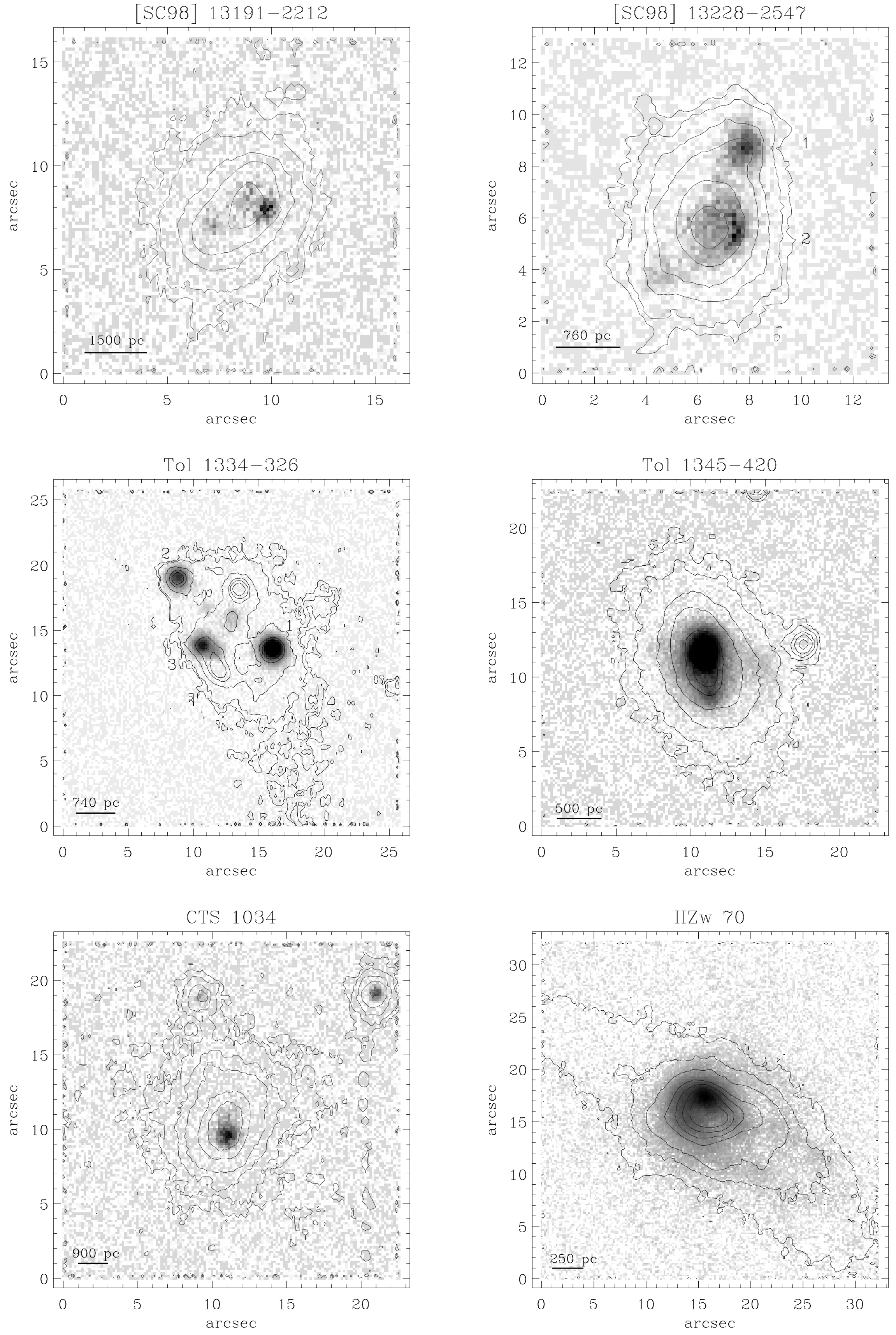

Fig. 4. continued.

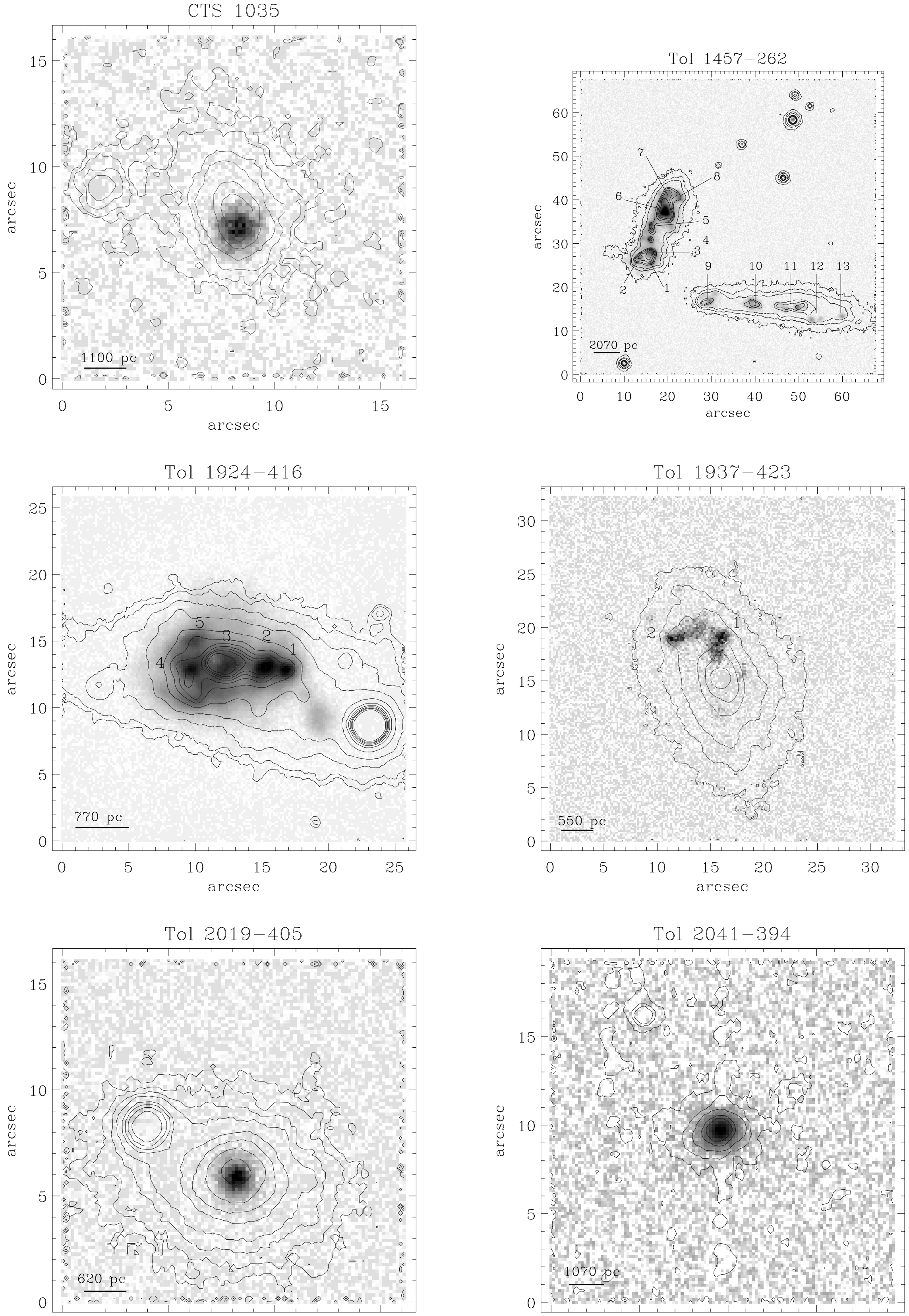

Fig. 4. continued.

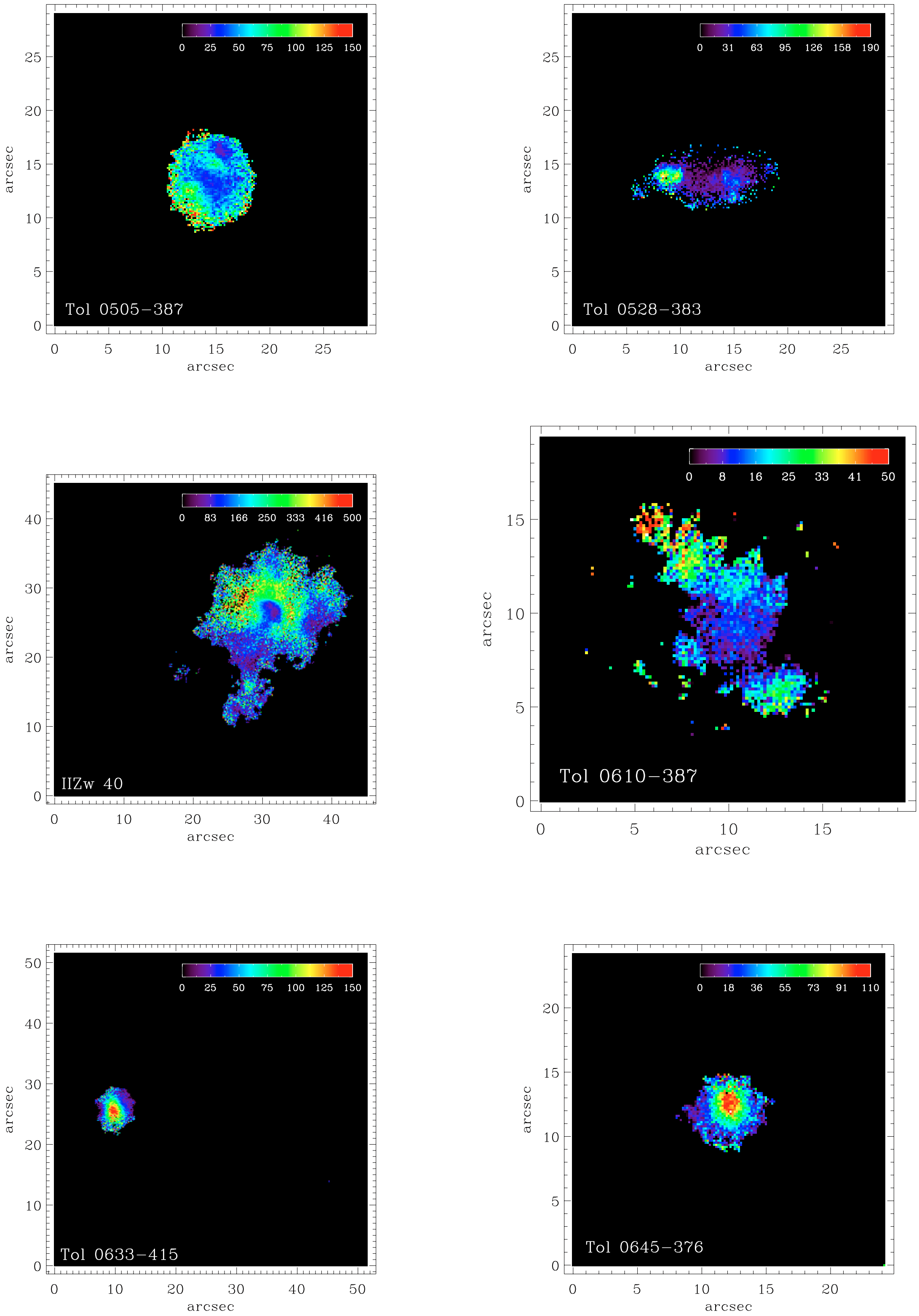

Fig. 5. Hβ equivalent width maps to our sample of HII galaxies. Colorbars in units of Å.

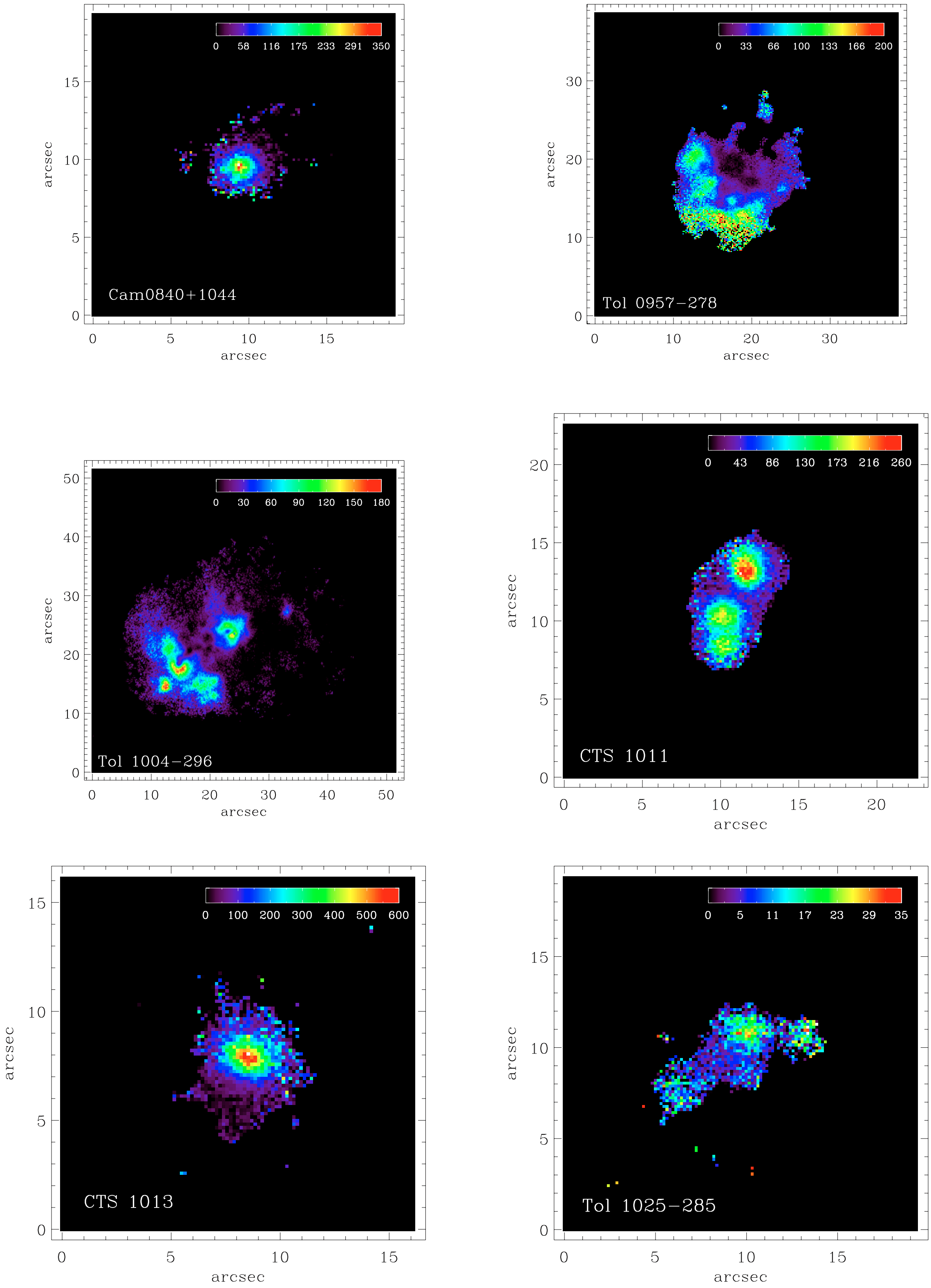

Fig. 5. continued.

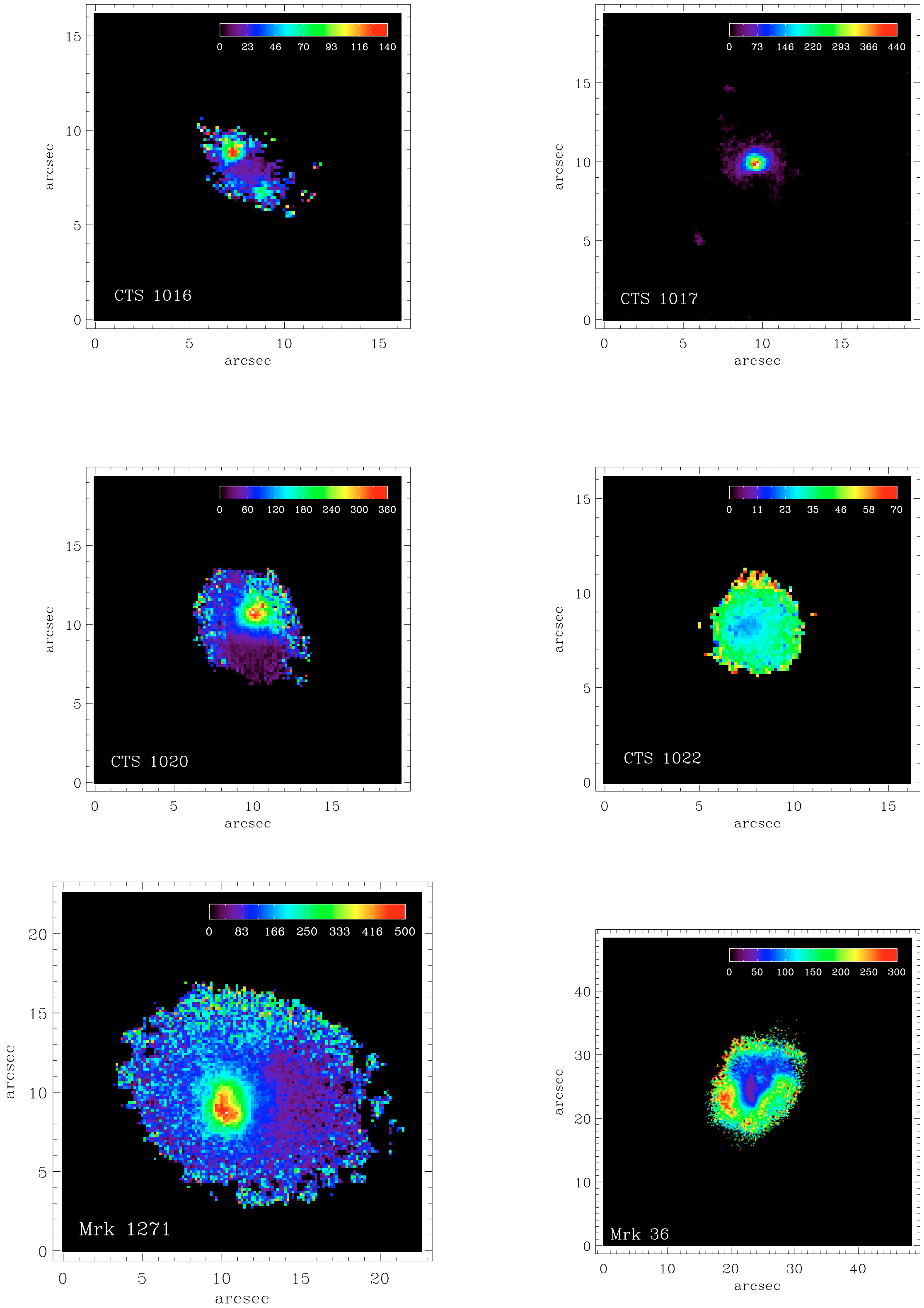

Fig. 5. continued.

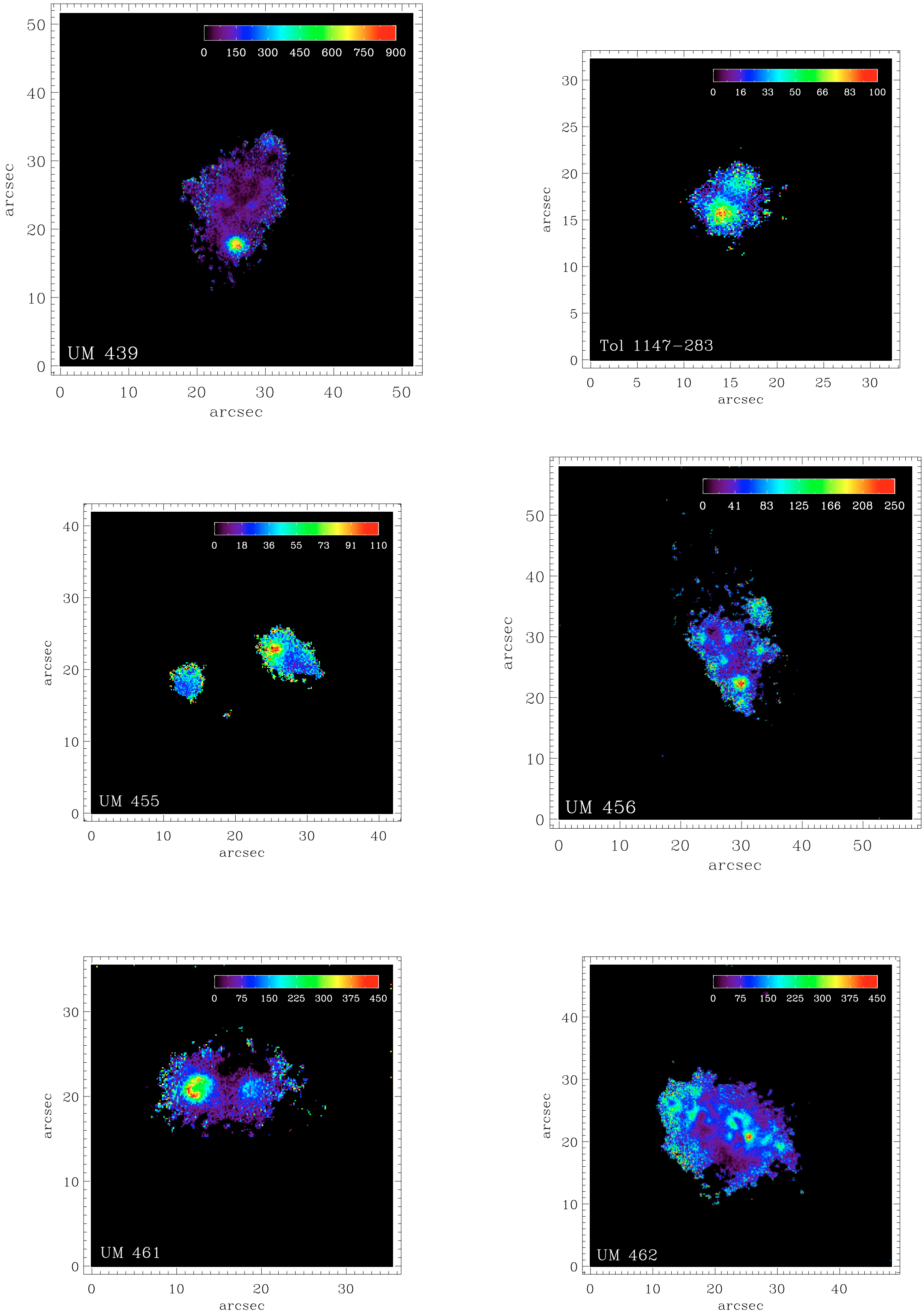

Fig. 5. continued.

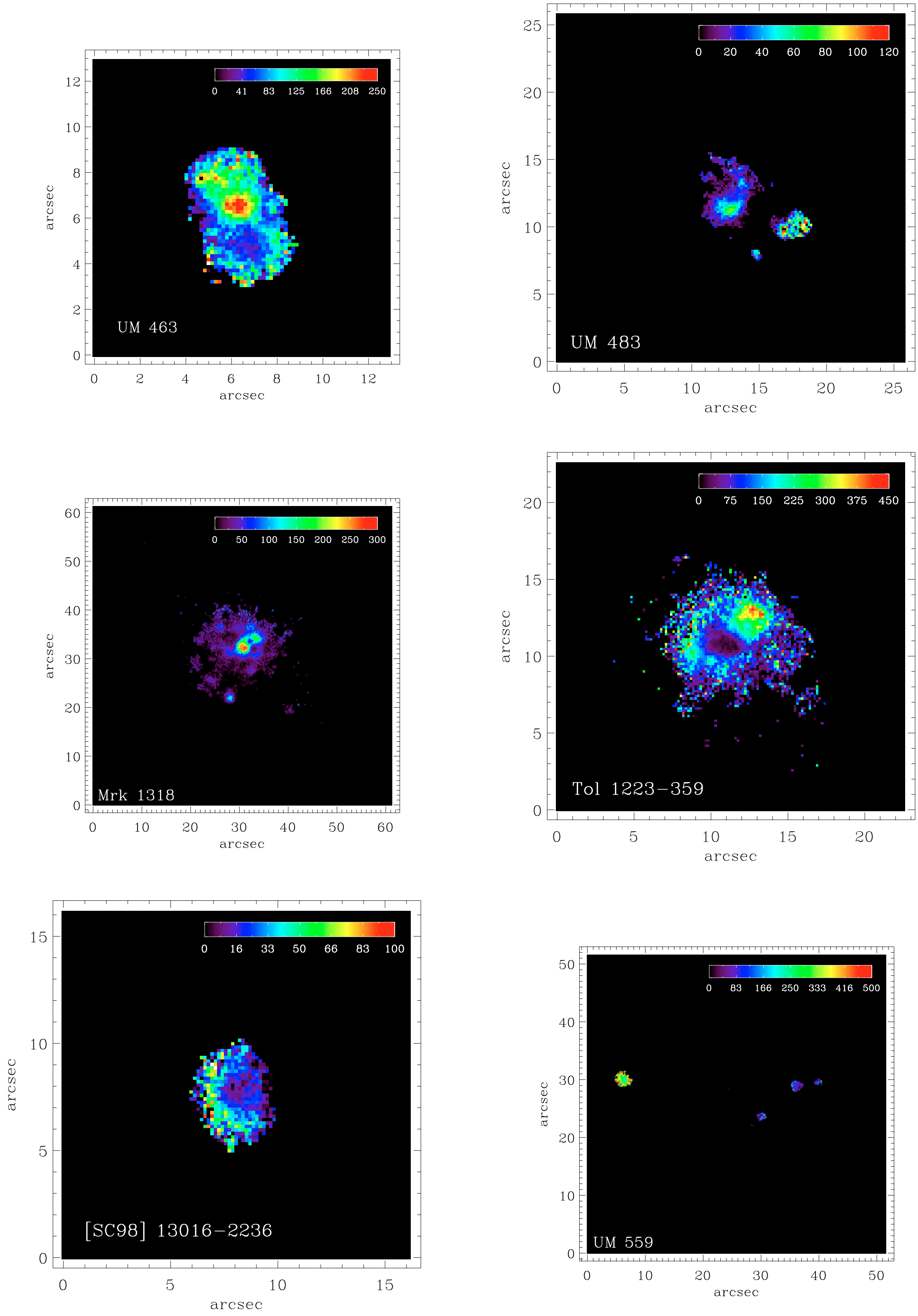

Fig. 5. continued.

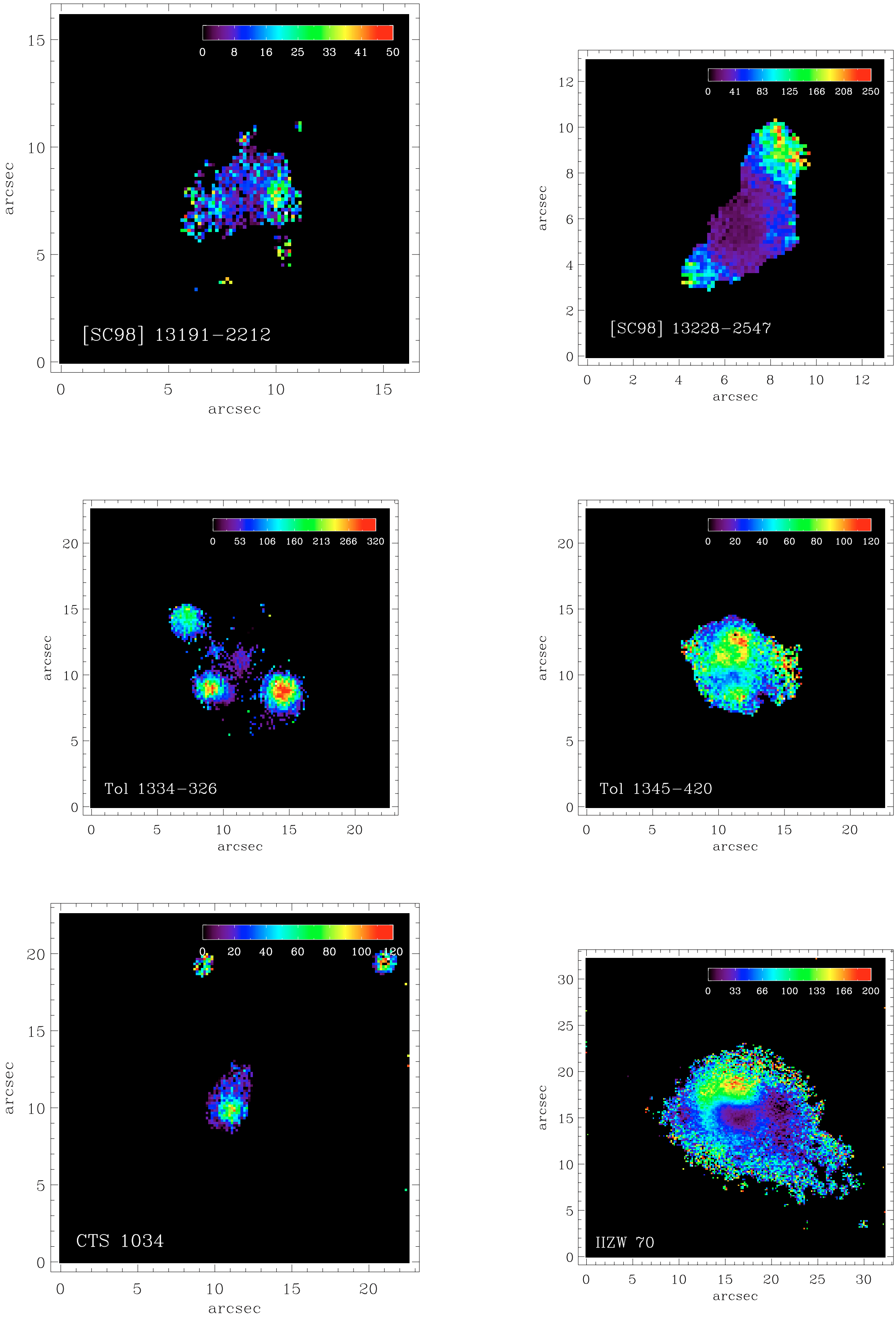

Fig. 5. continued.

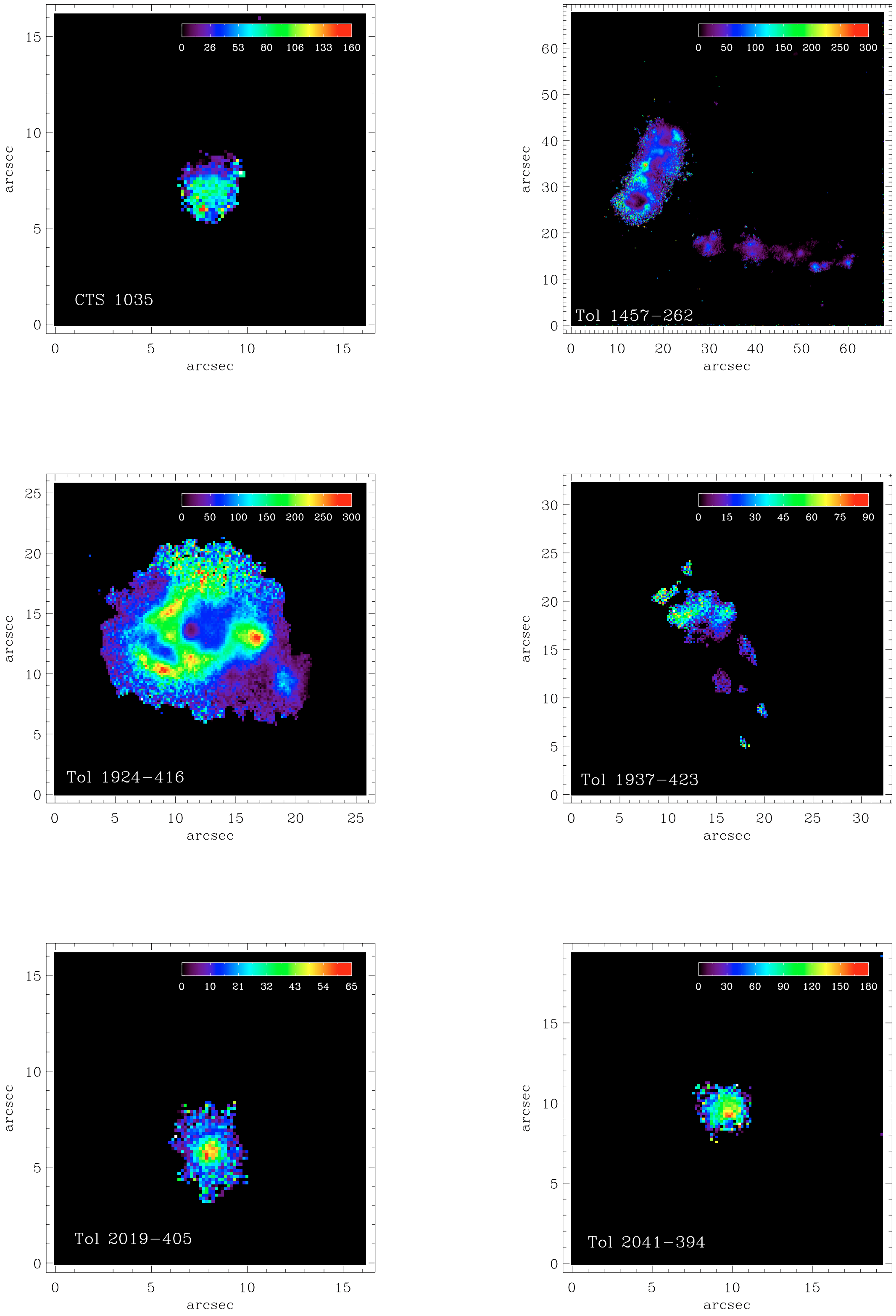

Fig. 5. continued.